JGR Space Physics

RESEARCH ARTICLE
10.1029/2022JA030675

Properties of Turbulent Alfvénic Fluctuations and Wave-Particle Interaction Associated With Io's Footprint Tail

S. Janser[1], J. Saur[1], G. Clark[2], A. H. Sulaiman[3], and J. R. Szalay[4]

[1]Institute of Geophysics and Meteorology, University of Cologne, Cologne, Germany, [2]Johns Hopkins University Applied Physics Laboratory, Laurel, MD, USA, [3]School of Physics and Astronomy, Minnesota Institute for Astrophysics, University of Minnesota, Minneapolis, MN, USA, [4]Department of Astrophysical Sciences, Princeton University, Princeton, NJ, USA

Key Points:

- Low-frequency Juno observations in the Io flux tube (IFT) tail represent structures perpendicular to background magnetic field
- Magnetic field fluctuations observed in the Io footprint tail (IFPT) are consistent with weak-MHD and sub-ion kinetic Alfvén wave turbulence
- Dispersion effects on group velocity of Alfvén waves widens the IFT consistent with the observed width of the IFPT

Correspondence to:
S. Janser,
janser@geo.uni-koeln.de

Citation:
Janser, S., Saur, J., Clark, G., Sulaiman, A. H., & Szalay, J. R. (2022). Properties of turbulent Alfvénic fluctuations and wave-particle interaction associated with Io's footprint tail. *Journal of Geophysical Research: Space Physics*, *127*, e2022JA030675. https://doi.org/10.1029/2022JA030675

Received 23 MAY 2022
Accepted 18 NOV 2022

The copyright line for this article was changed on 13 DEC 2022 after original online publication.

Abstract We investigate the small-scale magnetic field fluctuations and their associated turbulent nature in the Io flux tube (IFT) connected to Io's footprint tail (IFPT). Our study is based on the recent magnetic field measurements by the Juno spacecraft during the PJ12 Juno flyby. Here, we are interested in understanding what type of turbulence is consistent with the fluctuations in the quasi-dispersionless frequency range of 0.2–800 Hz as observed by Sulaiman et al. (2020), https://doi.org/10.1029/2020GL088432. Knowledge of the turbulent fluctuations is important to constrain the acceleration mechanisms for ions and electrons in the IFT. In this work, we suggest that the observed temporal fluctuations in the spacecraft frame correspond to Doppler-shifted spatial fluctuation structured perpendicular to the background magnetic field. This would imply an alternative reinterpretation of the spectral index of the observed magnetic power spectral density to be potentially the result of weak-MHD and sub-ion scale kinetic Alfvén wave turbulence in the low-frequency regime. Our theoretical modelings show that turbulence can be driven both in the torus region and at high-latitudes rendering results in agreement with the Juno measurements. Calculated turbulence heating rates are consistent with observed energy fluxes in the IFT and represent efficient drivers for particle acceleration. Moreover, a widening of the IFPT structure with respect to the IFT extent is consistent with propagating dispersive Alfvén waves modified by kinetic effects on their group velocities.

1. Introduction

Understanding the key physical aspects of the magnetospheric dynamics and related auroral emissions of Jupiter is a prime interest of the current Juno spacecraft mission. Juno's highly inclined low-perijove orbits with Jupiter flybys since 2016 give continually new insights into Jupiter's electromagnetic coupling to its magnetosphere. Besides the bright main auroral emissions and polar emissions, emissions related to the orbital motion of the Galilean satellites currently attract significant attention. In particular, Io's interaction with Jupiter is a topic of high interest since its discovery by Bigg (1964) via measurements of decametric radio emissions. In situ measurements from Voyager 1 and 2 Jupiter flybys in 1979 revealed flow (Belcher et al., 1981) and magnetic field (Acuna et al., 1981) fluctuations at Io, which are consistent with Alfvénic disturbances resulting from magnetospheric plasma streaming past Io. The unipolar inductor model (Goldreich & Lynden-Bell, 1969; Piddington & Drake, 1968) was the first theoretical model to describe the electromagnetic interaction and related power transmission in the Io flux tube (IFT). With the discovery of the dense Io plasma torus (Broadfoot et al., 1979), the Alfvén wing model (Neubauer, 1980) was established which highlighted the importance of the MHD Alfvén mode. This mode forms stationary Alfvén wings in the rest frame of Io and electromagnetically connects the satellite with Jupiter. Subsequent Galileo flybys of Io since 1995 and also remote sensing of IR (Connerney et al., 1993) and UV emissions (Clarke et al., 1996; Prangé et al., 1996) revealed more aspects of the complex local interaction and gave further observational evidence of the Io footprint emissions. The morphology of Io's auroral emissions comprises several features. The Main Alfvén wing (MAW) spot (Bonfond et al., 2008) is a result of Io's immediate plasma interaction by which the generated power is propagated via Alfvén waves to Jupiter. The understanding of the processes which lead to accelerated electrons and ions was only poorly constrained before the footprint and tail crossing of Juno. Pre-Juno theories for particle acceleration cover electric fields of inertial Alfvén waves at high-latitudes (Hess et al., 2010; Jones & Su, 2008), Alfvénic interaction in the torus region (Crary, 1997; Das & Ip, 1992), quasi-static field-aligned potential drops (Su et al., 2003) and also production of electron beams in the torus by repeated Fermi acceleration with Alfvénic electric fields. Moreover, there are emissions from transhemispheric electron beams, originating from the MAW of the other hemisphere (Bonfond et al., 2008). Further emissions are thought to come from Alfvén wave reflections inside the Io torus, considered

as reflected Alfvén wing spots (Connerney & Satoh, 2000; Jacobsen et al., 2007). The Io footprint tail (IFPT) completes the set of observed auroral emissions connected to Io and is related to field lines downstream of Io. The IFPT was proposed to be driven by quasi-static potentials accelerating electrons (Delamere et al., 2003; Hill & Vasyliūnas, 2002; Su et al., 2003). Alfvénic mechanisms were suggested alternatively (Bonfond et al., 2017; Crary & Bagenal, 1997).

Juno measurements shed new light on the high-latitude region associated with the IFPT. Infrared measurements from Mura et al. (2018) revealed a highly structured and partially bifurcated morphology of the IFPT, but the corresponding physics remains an open question. Based on observations of broadband electron energy distributions with power law like behavior and possible bi-directional characteristics in pitch-angle distributions (Szalay, Allegrini, et al., 2020; Szalay et al., 2018), current attention is now focused on an Alfvénic cause of the IFPT. This could be the same mechanism as for the MAW, potentially driven by reflections of Alfvén waves between the Io torus and Jupiter's ionosphere (Hess et al., 2010; Jones & Su, 2008). Also kinetic simulations from Damiano et al. (2019) encourage a dominating role of Alfvén waves to explain electron acceleration.

Surprisingly, accelerated upward proton populations were also detected by the JADE and the JEDI instrument (Clark et al., 2020; Szalay, Bagenal, et al., 2020). These charged particle detectors are sensitive to energy ranges of 50 eV–100 keV for JADE (McComas et al., 2017) and above for the JEDI instrument (Mauk et al., 2017), respectively. The data provide evidence of perpendicular ion heating in regions of expected electron acceleration above Jupiter, but also near the torus boundary, and is discussed in the realm of wave-particle interaction such as ion cyclotron resonance (Clark et al., 2020; Sulaiman et al., 2020; Szalay, Bagenal, et al., 2020). The importance of wave-particle interaction for the Io-Jupiter system and the IFPT was recently further highlighted by Sulaiman et al. (2020), who analyzed highly resolved magnetic field (MAG instrument, see Connerney et al., 2017) and electric field (Waves instrument, see Kurth et al., 2017) data of the PJ12 flyby. This flyby was identified as a potential MAW-crossing by Szalay, Allegrini, et al. (2020) based on observed intense electron energy fluxes of 580 mW/m^2. In this study, we will call this region IFT tail and is associated with field lines connected to the IFPT. Sulaiman et al. (2020) reported on electric and magnetic field perturbations in the frequency ranges of 0.2–3 Hz and 50–2 $\times$ 10^4 Hz from the MAG and Waves instrument, respectively. In particular, the frequency range up to 800 Hz shows no dispersion in the frequency-time spectrograms and also nearly transverse electric and magnetic field fluctuations with respect to the background magnetic field as expected for Alfvén and ion cyclotron waves (Sulaiman et al., 2020). The corresponding power spectrum of the magnetic fluctuations revealed a power law of spectral index -2.35 ± 0.07 up to 800 Hz. The observed fluctuations were interpreted as variations due to the parallel wavenumber with respect to the background magnetic field. Gershman et al. (2019) also derived a parallel spectral index of -2.29 ± 0.09 for MAG measurements (0.2–5 Hz) connected to the main emissions, which the authors attributed to strong turbulence.

In our study, we investigate the observed magnetic field fluctuations with the assumption that they can be described by turbulence models. We specifically consider Alfvénic turbulence generators located within the Io torus and outside the torus at high-latitudes. Understanding the nature of the fluctuations is important as these fluctuations can cause wave-particle interaction responsible for the accelerated electrons and ions of the IFPT. These acceleration processes highly depend on the temporal and spatial characteristics of the turbulent wavefield. With the help of the Juno measurements, we constrain the parameter spaces relevant for modeling of wave-particle interaction processes. Therefore, we estimate and compare basic spatial and temporal scales associated with the PJ12 flyby in Section 2. In Section 3, we motivate Alfvénic turbulence in the IFT based on the measurements and discuss different source locations of turbulence. Based on the findings from Section 2, we construct wavenumber spectra to characterize the wavevector structure of the Alfvénic fluctuations in the IFPT in Section 4. In the subsequent section, we provide evidence for the importance to account for Doppler shifting in Alfvénic turbulence and discuss implications of different turbulence models on the resulting observable frequency ranges in comparison to the presented observations of Sulaiman et al. (2020). We complete the discussion with a comparison of the associated theoretical power spectral indices and related Alfvénic power fluxes with the observations in Section 6.

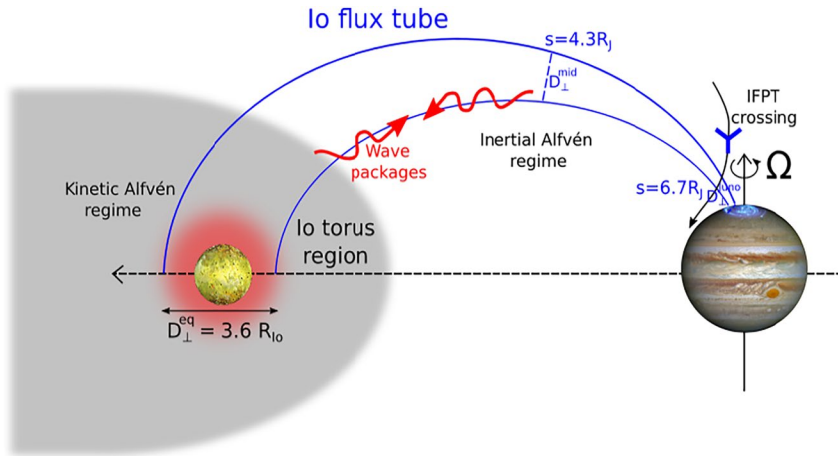

Figure 1. Overview of the Io-Jupiter system (not to scale). The Io flux tube connected to Jupiter transports energy to the high-latitude region via Alfvén waves. We consider two locations of Alfvénic turbulence activity, which are indicated with superscripts eq (equatorial, within the Io torus) and mid (mid-latitude, outside the Io torus). The distance along the flux tube is denoted by variable s (counted from equator in units of the Jupiter radius R_J). These locations distinguish each other regarding the plasma parameters, the width of the flux tube $D_\perp$, and thus also in Alfvénic dispersion characteristics (kinetic vs. inertial limit). The equatorial extent of the Io's interaction region is estimated to $D_\perp^{eq} = 3.6\ R_{Io}$ based on Saur et al. (2013). The resulting wavefield at the location of the IFPT measurements in the high-latitudes has a width $D_\perp^{Juno}$.

2. General Setup and Basic Temporal and Spacial Scales

Our study of turbulence in the IFT tail is motivated by the observation of a power law-like behavior of the magnetic power spectral density (Sulaiman et al., 2020) and the similarities with the main aurora (Gershman et al., 2019). Moreover, turbulence is also observed in the vicinity of Io and also in the middle magnetosphere based on Galileo data (Chust et al., 2005; Saur et al., 2002; Tao et al., 2015). From a theoretical perspective, we expect turbulence in the IFT due to wave reflections at strong gradients in Alfvén velocity, that is, at the Jovian ionosphere and possibly at the torus boundary (Hess et al., 2010). Counter propagating Alfvén waves generated by Io's interaction with the torus plasma interact via wave-wave interactions and establish a turbulence cascade. In the remainder of the paper, we investigate the implications for the current Juno observations from turbulence generator regions inside and outside the Io torus and various turbulence models.

In order to assess turbulence in the IFT, we start with a basic characterization of relevant time and length scales of the Alfvénic wavefield in this section. These scales help to analyze temporal and spatial Alfvén wave patterns contained in the IFPT observations of Sulaiman et al. (2020).

2.1. General Setup

An overview of the general setup used in this work is presented in Figure 1. Io acts as an obstacle to the overtaking torus plasma (with $v_0 = 57$ km/s) and provides the energy for the generation of Alfvén waves and eventually for turbulence. This interaction significantly alters the plasma flow around Io and causes velocity disturbances at various scales. These disturbances in turn cause magnetic field perturbations, which both propagate as Alfvén waves along the background magnetic field lines toward the high-latitudes. As a result of the inhomogeneity of the background plasma parameters along the flux tube, they transform into kinetic/inertial Alfvén waves. In this paper, we use the terminology kinetic Alfvén wave (KAW) equivalently to other publications, for example, Lysak and Lotko (1996) and Saur et al. (2018), to indicate small-scale Alfvén waves regardless of their kinetic effects and considered limits. The primary waves generated at Io are referred to as MAW and propagate in both hemispheres. On large scales, they are standing waves in the rest frame of Io.

Juno crossed the IFPT in the high-latitudes at a speed of 51 km/s during PJ12 (Sulaiman et al., 2020). The corresponding width of this structure is connected to the equatorial region via Jupiters' background magnetic field lines. Its equatorial extent is an indicator for the size of Io's interaction region at least for a direct MAW crossing and will be discussed in the next paragraph. The equatorial size of the mapped structure is larger than in the

high-latitudes as a consequence of the magnetic field topology, which we assume for simplicity to be dipolar in the analysis of this paper. The converging character of the flux tube toward the location of the Juno measurements is indicated in Figure 1.

2.2. Temporal and Spatial Scales in the Observed IFPT From PJ12

From the electric and magnetic field spectrograms from Sulaiman et al. (2020), we can conclude that Juno spent $T_{Juno} = 19 \pm 1$ s in the IFPT structure. This corresponds to a minimal detectable frequency in the spacecraft frame of $f_0^{sc} = \frac{1}{T_{Juno}} = 0.05$ Hz, which is within a factor of two in accordance with the processed magnetic power spectrum from Sulaiman et al. (2020). An estimation based on the set in of significant particle flux densities from the JADE instrument gives a reduced duration of $T_{Juno} = 17 \pm 1$ s (Szalay, Allegrini, et al., 2020). The crossing trajectory of the structure can be estimated to $D_{Juno} = 969$ km based on the spacecraft speed of $v_{sc} = 51$ km/s. Considering the tilt of the crossing according to Figure 1 in Sulaiman et al. (2020), we estimate the width of the IFPT to $D_{\perp}^{Juno} = 668$ km assuming an infinitely extended plate representing the flux tube tail. The corresponding equatorial cross section has an extent of $D_{\perp}^{eq} = 4.7\, R_{Io}$ ($R_{Io} = 1{,}822$ km), calculated by employing conservation of magnetic flux in a dipolar magnetic flux tube. Measuring the width of the tail in the infrared observations of Mura et al. (2018) and mapping it to the equator, we find a maximal equatorial scale of $D_{\perp}^{eq} = 5.3\, R_{Io}$. These results are similar to the estimates of Szalay, Allegrini, et al. (2020), who found variations of the equatorial width from IFPT crossings depending on Alfvén wave travel times and related longitudinal separations from the MAW.

2.3. Theoretical Temporal and Spacial Scales in the Io Flux Tube

Now we estimate the IFPT width based on expectations of the size of Io's interaction region. We start from the physical notion that Io's interaction with the streaming co-rotational torus plasma defines the largest perpendicular scale at which energy is injected to the system and thus shapes the generated Alfvén wavefield. Based on Saur et al. (2013), we consider an equatorial interaction scale of $3.6\, R_{Io}$ due to Io's ionospheric extent and the extended region of increased Poynting flux at the flanks of the Alfvén wing. Exploiting conservation of magnetic flux within a flux tube, we estimate the IFPT width to $D_{\perp}^{Juno} = 513$ km at the location of measurement. The tilted Juno trajectory can be calculated to $D_{Juno} = 749$ km. The corresponding Juno flight time through this structure is:

$$T_{Juno} = \frac{D_{Juno}}{v_{sc}} \approx 15\ s. \tag{1}$$

The deviation between the theoretically estimated flux tube cross-section and the observed width of the IFPT indicates that further effects widen the structure. In the context of turbulence and associated small-scale Alfvén waves within the Alfvén wing, dispersion might be a conceivable explanation for the deviations as well. From calculations shown in Section 4.2, we estimate the potential effect of dispersion on swept perpendicular distances of the waves up to several hundred kilometers in the high-latitudes on ion gyroradius scales.

Now we turn to the question of physical time scales associated with the Io interaction. The convection time, that is, the time it takes the co-rotating torus plasma to pass Io, is given by:

$$T_{conv} = \frac{3.6 R_{Io}}{v_0\,(1 - \bar{\alpha})}, \tag{2}$$

where $\bar{\alpha}$ describes the interaction strength at Io, that is, how strongly the unperturbed plasma flow ($v_0 = 57$ km/s) is slowed (cf. e.g., Saur et al., 2013). The induced velocity perturbations propagate as Alfvén waves with an associated magnetic field amplitude δB along the field lines. As a result of the increasing Alfvén velocity toward Jupiter, their spatial wavelengths grow in parallel direction. Even if this wavefield propagates nearly at the speed of light in the high-latitudes, the slowest temporal variability in a frame moving with the plasma is still linked to the convection time T_{conv}.

As the plasma velocity at the flanks and the center of the Alfvén wings are different, we represent the associated convection time by values for $\bar{\alpha} = [0, 0.9]$ to cover both regions. We choose the strong interaction strength $\bar{\alpha} = 0.9$ according to Blöcker et al. (2018) and Saur et al. (2013), whereas the limit $\bar{\alpha} = 0$ constitutes the case of the unperturbed plasma flowing at speed v_0 past Io. We obtain values for T_{conv} ranging between 115 and 1,150 s. Comparing these values to the crossing time from Equation 1, we can conclude that the observed low-frequency

fluctuations correspond to the time scales of the IFPT crossing and not to the temporal variability caused by Io. Thus, we infer that Juno flew through a quasi-static wavefield structure concerning the largest scales, that is, the instruments cannot sense large-scale temporal variability of the wavefield in the spacecraft frame during a crossing of 19 s. Only temporal variations in plasma frame on period scales smaller than T_{Juno} can be detected by the MAG and Waves instrument on-board of Juno. This gives us an upper-frequency limit $f_0^{sc} = \frac{1}{T_{Juno}} = 0.05$ Hz to interpret the data as being dominated by spatial patterns. This does not mean, that for higher frequencies automatically temporal variations dominate the observable signal as will be shown in the next sections. In summary, we conclude that for the largest wave scales within the flux tube Taylor's frozen-in-field hypothesis holds in the high-latitude region. Taylor's hypothesis says that observed temporal variations are caused by advected spatial structure if the advection velocity is sufficiently large (e.g., Frisch, 1995). This applies generally for many spacecraft measurements such as in the solar wind (e.g., Howes et al., 2014), Jupiter's equatorial magnetosphere (Saur et al., 2002) or Saturn's equatorial magnetosphere (von Papen et al., 2014).

Finally, we characterize the structure of the wavefield parallel to the background magnetic field in the equatorial region. The dispersion relationship for the MHD Alfvén wave provides a link between the maximum parallel wavelength generated at Io and the convection time scale via $\lambda_{\parallel}^{\max} = T_{conv} \cdot v_A^{Io}$. This relation allows us to estimate the largest possible parallel wavelength to $\lambda_{\parallel}^{\max} = [0.3, 3.3] \cdot R_J$ near Io for both convection time scales using an Alfvén speed of $v_A^{Io} = 200$ km/s (Kivelson et al., 2007) and the equatorial Jupiter radius $R_J = 71{,}492$ km. Thus, the wavefield is elongated in the parallel direction, which is important for the existence of KAWs.

3. Alfvénic Turbulence in the Io Flux Tube Tail

In this section, we motivate the turbulent Alfvénic nature of the observed fluctuations in the IFPT and characterize the turbulence at different source locations in- and outside the torus region.

3.1. Alfvénic Nature of the Observed Fluctuations

We focus on the observed (non- and weakly dispersive) lower-frequency regime from the MAG and Waves data presented in Sulaiman et al. (2020), that is, in the spacecraft frequency range of $f^{sc} = \frac{\omega^{sc}}{2\pi} = [0.2, 800]$Hz. We assume the associated fluctuations to be at least partially Alfvénic based on the established nature of the IFT in the literature close to Io (Acuna et al., 1981; Neubauer, 1980). This is also supported by the mainly perpendicular fluctuations in electric and magnetic field components as observed by Sulaiman et al. (2020). Sulaiman et al. (2020) suggested that the investigated frequency range of the magnetic power spectral data might be connected over a single power law. The authors found a spectral index of $\alpha = -2.35 \pm 0.07$, which they interpret in association to the findings of Gershman et al. (2019) for the main auroral emissions as partially developed critically balanced strong MHD turbulence. In this case, the power spectral density exhibits a $P_{\perp} \sim k_{\parallel}^{-2}$ behavior (Goldreich & Sridhar, 1995; Horbury et al., 2008), based on their assumption that the measured frequencies map to the parallel wavenumber $k_{\parallel}$. However, instead of an interpretation of a $k_{\parallel}$ spectrum, we will show in Section 5 that the observed spectrum is consistent with a Doppler-shifted $k_{\perp}$ turbulence spectrum. As we will see in Section 4, this means that Juno observed a nearly static wavefield with no temporal changes.

3.2. Turbulence Generator Regions

As indicated in the beginning of Section 2, waves reflect at strong gradients in Alfvén velocity, that is, at the ionosphere and at the torus boundary. Counter-propagating waves can establish a turbulent cascade via nonlinear wave-wave interactions and cause a filamentation process. In the case of strong turbulence, a single "collision" is sufficient for a significant deformation of the involved wave packets. For a weak turbulent process, several wave-wave interactions are required for the same effect. The corresponding magnetic fluctuation amplitudes are small compared to the background field in this case.

In the following, we take two distinct regions for the development of turbulence into account, inside and outside of the Io torus (see Figure 1). We do so because these regions are characterized by different turbulence natures as we will see in the next subsection. Outside the torus, the turbulence properties also depend on the waves interference region along the field line. Thus, we choose two turbulence generator locations as representatives for both turbulence cases, although turbulence generally is allowed to develop everywhere outside the torus. The

first location is placed in between the torus boundary and the ionosphere at 4.3 R_J from the equator, in Figure 1 indicated as "mid." The second is located directly at the location of measurement in the high-latitudes. At small sub-ion scales, turbulence is generally characterized as strong and thus, kinetic turbulence is possible at both regions as a result of shrinking non-linear time scales.

3.3. Characterization of the Turbulence Nature

The turbulent nature in the IFT can be assessed by comparing involved interaction time scales. The dimensionless parameter $\epsilon = \tau_A/\tau_{nl}$ characterizes whether turbulence is strong or weak, with $\epsilon > 1$ for strong turbulence and $\epsilon < 1$ for weak turbulence (see e.g., Saur et al., 2002). The characteristic interaction time of Alfvén waves in the torus region is $\tau_A = \int_{-2R_J}^{2R_J} v_A^{-1}(s)ds = 573\,\mathrm{s}$. The eddy turnover time as a measure for the deformation of a Alfvén wave package is characterized by a spatial change on order of the perpendicular wavelength $\lambda_\perp^{\max}$ of the Alfvén wave package at a rate of the velocity fluctuation $\delta v_A = \frac{\delta B}{B_0} v_A$. Thus, this time scale is $\tau_{nl} = \frac{\lambda_\perp^{\max}}{\delta v_A} = \frac{\lambda_\perp^{\max}}{v_A}\frac{B_0}{\delta B}$, where $\lambda_\perp^{\max} = 3.6 R_{Io}$ describes the largest perpendicular scale in the Io torus. Using an Alfvén velocity of 200 km/s (Kivelson et al., 2007) and a ratio of $\frac{B_0}{\delta B} \approx 5$ for the largest wave amplitude (Kivelson et al., 1996), we can estimate the nonlinear time scale to $\tau_{nl} = 164$ s close to Io. In conclusion, the ratio $\epsilon = \frac{\tau_A}{\tau_{nl}} = 3.49$ is slightly larger than one and indicates a strong turbulent interaction in the torus region. However, we like to note that the plasma parameters close to Io can temporally vary as a result of Io's position inside the torus or variable atmospheric conditions and thus might influence the time scales and the character of occurring turbulence. A decreased particle density leads to an enhanced Alfvén velocity and consequently to a reduced Alfvén time. Meanwhile, the nonlinear time increases and finally might push ϵ below one and temporarily allow for weak turbulence in the torus region. Also, considering a reduced magnetic field perturbation according to Chust et al. (2005) of $\delta B^{rms} = 100$ nT would even lead to $\epsilon = 0.87$.

Now, we turn our attention to turbulence generator regions outside the torus. Estimation of the time scales similar to the torus region gives $\tau_A = \int_{2R_J}^{7R_J} v_A^{-1}(s)ds \approx 15\,\mathrm{s}$, and $\tau_{nl} = \frac{\lambda_\perp}{v_A}\frac{B_0}{\delta B} = 6.5\,\mathrm{s}$ for a location in the middle between the torus boundary and the ionosphere. We used a perpendicular scale of $\lambda_\perp = 2{,}430$ km according to the scale mapping within the flux tube as used in Section 2. The Alfvén speed and dipole magnetic field strength are $v_A = 0.37c$ and $B_0 = 1.5 \times 10^{-5}$T according to the field line models from Su et al. (2006). The fluctuation amplitude is estimated to $\delta B = 50$ nT exploiting the conservation of energy flux. The resulting time scale ratio is $\epsilon = 2.3$ and thus favors a strong turbulent process. However, if we place the turbulence generator toward the location of the Juno measurements in the high-latitudes, we obtain a nonlinear time scale of $\tau_{nl} = 18$ s and consequently, $\epsilon = 0.83$. The quantities used for this estimate are $\frac{B_0}{\delta B} \approx \frac{3{\cdot}10^5 nT}{30nT}$, $v_A = 0.96c$ and $\lambda_\perp = 513$ km. The Alfvén speed is taken from Sulaiman et al. (2020). The fluctuation amplitude associated with turbulence is estimated by integration of the observed power spectrum from $f = 0.05$–800 Hz. We observe that the location of the turbulence generator outside the torus influences the timescale ratio and also allows for weak turbulence conditions.

In Section 5, we analyze the temporal variability of the observed wavefield from Juno's IFPT crossing, now explicitly considering the higher wave frequencies due to Alfvénic turbulence. The large-scale temporal and spatial estimates of the wavefield from Section 2 help to constrain the parameter ranges for the parallel and perpendicular wavenumbers, which are needed for modeling. The corresponding theoretical basics are presented in the next section. Based on the respective turbulence nature at the various generator regions, we apply three different turbulence models in this paper: two MHD models, considering weak as well as strong wave-wave interaction, and a sub-ion scale KAW turbulence approach. The relevant information regarding the investigated models are summarized in Table 1. We like to note, even though the measurements indicate that the electric fluctuations have a primarily transverse nature, it is still reasonable to take KAW turbulence into consideration. The KAW's parallel electric field $\delta E_\parallel$, which is absent in the MHD regime, develops a field strength at least two orders of magnitude lower than the perpendicular field component $\delta E_\perp$ at smallest perpendicular scales in the high-latitudes for the strong interaction strength $\bar{\alpha} = 0.9$. Even for a weak interaction with a limit of $\bar{\alpha} = 0$, $\delta E_\parallel$ is still an order of magnitude smaller than $\delta E_\perp$ as $\delta E_\parallel$ scales with $k_\parallel$ with respect to $\delta E_\perp$ (Borovsky, 1993). Hence, Juno still observes nearly transverse electric field signatures in case of KAWs.

Table 1
Considered Turbulence Models in the Io Flux Tube

Description	$P(k_\perp) \propto k_\perp^\alpha$	Wavenumber relation	Authors
Strong (anisotropic) MHD turbulence	$\alpha = -5/3$	$k_\parallel = a_1^{strong} k_\perp^{2/3} L^{-1/3}$	Goldreich and Sridhar (1995)
Weak MHD turbulence	$\alpha = -2$	$k_\parallel = a_1^{Weak} \frac{\delta B}{B_0} k_\perp^{1/2} k_0^{1/2}$	Galtier et al. (2000), Ng and Bhattacharjee (1997), and Saur et al. (2002, 2018)
(Sub-ion scale) Kinetic Alfvén wave (KAW) turbulence	$\alpha = -7/3$	$k_\parallel = a_2^{KAW} k_\perp^{1/3} \rho_i^{-1/3} L^{-1/3}$(MHD-breakdown at ρ_i) $k_\parallel = a_2^{KAW} k_\perp^{1/3} \lambda_i^{-1/3} L^{-1/3}$(MHD-breakdown at λ_i)	Howes et al. (2008) and von Papen and Saur (2015)

Note. The perpendicular power spectral index is denoted by α (not to confuse with the interaction strength $\bar{\alpha}$). L describes the largest scale at which the energy is injected into the system and is chosen here to be equivalent to the effective diameter of Io, that is, $3.6R_{Io}$, for equatorial turbulence. Anisotropy factors a_1 and a_2 account for the anisotropic nature of the wavefields close to Io.

4. Wavenumber Spectra Based on Turbulence Theories

In the following, we further investigate the spatio-temporal structures of the fluctuations. As discussed in Section 3, the interpretation of the observed power law in the magnetic power spectrum regarding its implied turbulence physics depends on the spatial and temporal structure of the observed frequencies.

4.1. Doppler Shifting

For the interpretation of the IFPT Juno measurements we consider three different frames of reference. In the Io rest frame, the Alfvén waves are stationary on large scales. Thus, the large scale wave fluctuation quantities such as current density $\delta\vec{j}$, electric field $\delta\vec{E}$ and magnetic field $\delta\vec{B}$ do not change with time along the Alfvén characteristics. In the literature, the terminology "standing Alfvén wing" is commonly used (e.g., Neubauer, 1980) and thus is characterized with a frequency of $\omega^{Io} = 0$ in the Io rest frame. The superscript indicates the frame of reference to which the considered quantity is related to. In the frame rotating with Jupiter's magnetospheric plasma, that is, the plasma rest frame, the Alfvén waves fluctuate at their intrinsic frequency ω^B. This frequency is described by dispersion relationships, such as $\omega^B\left(\vec{k}\right) = k_\parallel v_{A,rel}$ in the MHD regime or approximations like

$$\omega^B\left(\vec{k}\right) = k_\parallel v_{A,rel}\sqrt{1 + k_\perp^2\left(\rho_s^2 + \frac{3}{4}\rho_i^2\right)} \tag{3}$$

in the kinetic limit and

$$\omega^B\left(\vec{k}\right) = \frac{k_\parallel v_{A,rel}}{\sqrt{1 + k_\perp^2 \lambda_e^2}} \tag{4}$$

in the inertial limit (Lysak & Lotko, 1996). The semi-relativistic Alfvén speed is denoted by $v_{A,rel} = \frac{v_A}{\sqrt{1+\left(\frac{v_A}{c}\right)^2}}$, where $v_A = \frac{B_0}{\sqrt{\mu_0 m_i n}}$ is the classic Alfvén speed. The corresponding plasma length scales, that is, ion gyroradius, ion-acoustic gyroradius, and electron inertial length, are indicated by ρ_i, ρ_s, and λ_e. The kinetic limit considers thermal effects on the wave frequency and is appropriate in the torus region, whereas the inertial limit considers effects from electron inertia and is applicable in the high-latitudes. The third frame of reference is the Juno spacecraft frame, in which the Juno measurements were obtained in the high-latitudes. This frame moves relative to the other frames and observes the wavefield at frequencies ω^{sc}.

To relate the frequencies in the relatively moving frames of reference, we start with the general Doppler expression given by numerous authors (e.g., Howes et al., 2014) as:

$$\omega^{sc} = \omega + \vec{k}\cdot\vec{v}_{rel}. \tag{5}$$

Here, ω^{sc} is the frequency observed in a frame (e.g., a spacecraft frame of reference) moving at velocity $-\vec{v}_{rel}$ relative to an other frame. The latter frame is the plasma rest frame where the wave fluctuates at its intrinsic

frequency ω and is associated with a wavevector $\vec{k}$. We apply this expression to the introduced frames of reference and illustrate the effect on the observed frequency. At first, we consider only large-scale Alfvén waves, that is, in the limit of the standing Alfvén wing and thus $\omega^{Io} = 0$.

The Io and plasma rest frame move relative to each other at a speed of $v_B^{Io} = -v_{Io}^B = 57$ km/s at Io's orbital position. An observer moving with the plasma frame would observe the standing Alfvén wing as spatially convected (Doppler shifted) wavefield with a "convection" frequency $\omega^B = \omega^{Io} + \vec{k} \cdot \vec{v}_{Io}^B = \vec{k} \cdot \vec{v}_{Io}^B$ (Neubauer, 1998).

The high-latitude Juno spacecraft would sense the standing Alfvén wing at frequencies $\omega^{sc} = \vec{k} \cdot \vec{v}_{Io}^{sc}$. This is a convection of the Alfvénic wavefield past the spacecraft in Juno's frame of reference similar to the equatorial example. Observing the same wavefield with respect to the plasma rest frame results in $\omega^{sc} = \vec{k} \cdot \left(\vec{v}_{Io}^{sc} - \vec{v}_{Io}^B\right) = \vec{k} \cdot \vec{v}_B^{sc}$. Thus, the wave fluctuations can be considered as frozen-in when they are convected over the Juno spacecraft.

Now we ask the question whether the Taylor hypothesis still holds if ω^{Io} deviates from zero as a result of turbulence or related to plasma conditions in the torus. Explicit time variation due to torus variability are on the convection time scales past Io or even longer, that is, the rotation period of Jupiter, which are significantly longer compared the Juno cross timing of 17 s. Hence, the latter variations are negligible in the interpretation of the Juno measurements. Therefore, we investigate role of temporal variations due to the evolution of turbulence in the IFT tail. In this case, we obtain a temporal contribution of the Alfvénic wavefield in the form $\omega^B = \omega^{Io} + \vec{k} \cdot \vec{v}_{Io}^B$ in the plasma frame, which results in

$$\omega^{sc} = \omega^B\left(\vec{k}\right) + \vec{k} \cdot \vec{v}_B^{sc} \tag{6}$$

for an observer moving with the spacecraft relative to the plasma frame at a speed of $v_{sc}^B = -v_B^{sc}$.

Putting Equation 6 in the context of the measurements reported during the PJ12 flyby by Sulaiman et al. (2020), the Juno instruments MAG and Waves measured fluctuating electromagnetic quantities of the spatio-temporal wavefield as $\omega^{sc}\left(k_\perp, k_\parallel, \omega^B\left(\vec{k}\right)\right)$ is a function of wavenumber vector $\vec{k}$ and wave frequency ω^B. We can further simplify expression (Equation 6) toward

$$\omega^{sc} \approx \omega^B\left(\vec{k}\right) + k_\perp v_B^{sc} \tag{7}$$

by considering Juno's highly inclined trajectory with respect to the local magnetic field, that is, $\vec{v}_{sc}^B \perp \vec{B}_0$. However, this approximation also holds for smaller angles because we assume the existence of (anisotropic turbulently cascaded) inertial Alfvén waves in the high-latitudes with $k_\parallel \ll k_\perp$ (see Section 3).

The idea of the following subsections is to investigate if ω^B is still negligibly small compared to $k_\perp v_B^{sc}$ in Equation 7 when a turbulent cascade evolves, that is, if the Taylor hypothesis still holds in the spacecraft frame for $k_\perp > k_\perp^{\min}$. In Section 2, we already demonstrated that the Taylor hypothesis holds for $k_\perp^{\min}$, which corresponds to the width of the IFT at location of the Juno crossing.

In the next step, we assume the dispersion relationship for inertial Alfvén waves from Equation 4 to represent ω^B in Equation 7, which leads to:

$$\omega^{sc} = \frac{k_\parallel v_{A,rel}}{\sqrt{1 + (k_\perp \lambda_e)^2}} + k_\perp v_B^{sc}. \tag{8}$$

We point out that the dispersion relation in Equation 7 holds exactly in infinite and homogeneous plasmas. It is a good assumption if the wavelengths are significantly smaller than the size of the system. Regarding the infinity assumption, we point out that in case of the IFT assuming $\omega^{Io} = 0$, Equation 4 implies that the parallel wavelength in the Io rest frame is infinite. This is formally possible if we include the reflection of the waves at Jupiter's ionosphere, leading to a formally infinite downstream pattern of reflected waves (see wave reflection in e.g., Kivelson et al., 2007; Neubauer, 1980). Returning to Equation 8, the negligibility of ω^B compared to $k_\perp v_B^{sc}$ at the largest scales implies that associated $k_\parallel^{\min}$ in Equation 8 needs to be formally so small that $k_\parallel^{\min} v_A^{rel} \approx k_\parallel^{\min} c \ll k_\perp^{\min} v_B^{sc}$.

The turbulent cascade evolves in the $k_\perp$ direction (Goldreich & Sridhar, 1995; Schekochihin et al., 2009), that is, $k_\perp$ of the fluctuations grows larger. The parallel turbulent scales follow the perpendicular cascade according to the

critical balance assumption, but the parallel scales do not drive it. Subsequently $k_\parallel$ grows as well, but generally slowlier than $k_\perp$ according to the critical balance assumption which is of the form $k_\parallel \sim k_\perp^\gamma$ with $\gamma < 1$. Therefore, the Taylor hypothesis is also expected to hold for $k_\perp$ larger than $k_\perp^{\min}$. In Sections 4.2 and 5, we will study these evolutions in detail, which additionally depend on the nature of turbulent cascade and the nonlinearities of the various dispersion relationships in the various plasma regimes.

Gershman et al. (2019) and Sulaiman et al. (2020) interpret the Juno measurements as true frequencies in the rest frame of the plasma based on the large wave velocity compared to the spacecraft speed. They conclude that Doppler shifting corrections are negligible (last term in Equation 8) and thus only interpret the observed frequency as temporal variations (wave frequency) according to the MHD dispersion relation for Alfvén waves, $\omega = k_\parallel v_{A,rel} \approx k_\parallel c$. This has a large impact on the interpretation of the magnetic power spectra regarding their nature of turbulence as discussed in Section 3. In the following, we will show that the Doppler shifted contribution in Equation 8 instead plays a dominant role for the interpretation of the measured frequencies.

4.2. Wavenumber Spectral Ranges

Having derived an expression for the observable frequencies in the spacecraft frame in the high-latitudes, we now introduce wavenumber spectral ranges for explicit modeling of generated fluctuation frequencies due to turbulence. Then, we relate these wavenumbers at their respective turbulence source locations to the high-latitudes as the generated Alfvén waves propagate in a converging magnetic field geometry.

We consider a spectral range for the equatorial (eq) perpendicular wavenumbers in the torus region as $k_\perp^{eq} = \left[\frac{2\pi}{3.6R_{Io}}, \frac{2\pi}{\rho_i^{eq}}\right]$, where the largest scale is related to Io's extended interaction region (see Section 2) and the smallest MHD scale is the equatorial ion gyroradius ρ_i^{eq}. At spatial scales comparable to the ion scales, a spectral break occurs, where the MHD turbulence turns into kinetic turbulence. However, there is an ongoing discussion in the literature about whether MHD turbulence turns into kinetic scale turbulence at the ion gyroradius or the ion inertial length scale λ_i (e.g., Chen et al., 2014; Franci et al., 2016). For the IFT, the decoupling of ions from the fluid motion as described by the ion inertial length might be especially interesting for turbulence in the high-latitudes due to increased importance of ion inertia as a result from very low ion plasma beta. The consequences of the breakdown at both scales on the resulting wave characteristics are investigated in the following sections. For the sub-ion scales, we consider a spectral range of $k_\perp^{eq} = \left[\frac{2\pi}{\rho_i^{eq}}, 10\frac{2\pi}{\rho_i^{eq}}\right]$ or λ_i^{eq} as smallest MHD scale, respectively. The largest wavenumber is chosen arbitrarily to cover sufficient parts of the considered frequency regime. For the rest of the paper, we refer to the "ρ_i-case" and "ρ_i-MHD model" to indicate the spectral break to occur at the ion gyroradius scale for the turbulence model under concern. Analogously, we use the term "λ_i-case" and "λ_i-MHD model" for the spectral ranges and associated turbulence models considering a spectral break at the ion inertial length λ_i. A given superscript (eq, mid, hl) refers to the turbulence source location inside (eq) or outside the torus (mid, hl).

Applying the wavenumber relations from the different turbulence models given in Table 1, we calculate the associated parallel wavenumbers needed to characterize the waves. We introduce anisotropy factors in the wavenumber relationships (see Table 1) to account for the anisotropic nature of the wavefield at largest scales, that is, at energy input scales. In this context, anisotropy refers to the elongated structure of the wave packages with $\lambda_\parallel > \lambda_\perp$ as a consequence of long plasma convection time. In particular, the MHD anisotropy factors a_1 are defined such that the largest perpendicular wavelength $\lambda_\perp^{\max}$ matches the largest parallel scale $\lambda_\parallel^{\max}$ as introduced in Section 2. Exemplary for the equatorial strong MHD turbulence model in Table 1, the anisotropy factor a_1^{strong} can be obtained from the minimum perpendicular and parallel wavenumbers (see Section 2) of the form

$$k_{\parallel,eq}^{\min} = \frac{2\pi}{T_{conv}(\bar{\alpha}) \cdot v_A^{Io}} = k_\parallel^{strong}\left(k_{\perp,eq}^{\min}\right) = a_1^{strong} \cdot \left(k_{\perp,eq}^{\min}\right)^{2/3} L^{-1/3}, \tag{9}$$

where $k_{\perp,eq}^{\min} = \frac{2\pi}{3.6R_{Io}}$ is the largest perpendicular scale. The kinetic anisotropy factors a_2 are defined equivalently, now over the parallel wavenumber of the respective MHD turbulence model at its breakdown scale to smoothly connect the MHD and the kinetic regime.

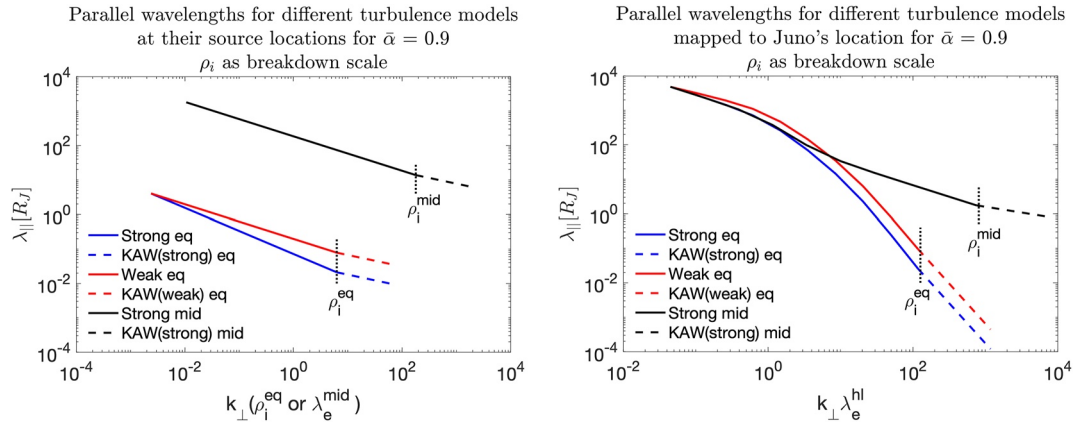

Figure 2. Parallel wavelengths (for $\bar{\alpha} = 0.9$) plotted against perpendicular scale based on turbulence originating at different locations with ion gyroradius ρ_i as MHD-breakdown scale. The horizontal axis considers the perpendicular wavenumber normalized to the local ion gyroradius for the equatorial models (eq) and the electron inertial length for the models with a source location outside the torus (mid). Left: spectra at the respective source locations. Right: mapped spectra to the location of the Juno measurements in the high-latitudes.

The resulting set of wavenumbers $\left(k_{\perp}^{eq}, k_{\parallel}^{eq}\right)$ are mapped along the flux tube toward the location of measurement in the high-latitudes (superscript hl). The perpendicular scale maps according to

$$k_{\perp}^{hl} = k_{\perp}^{eq}\sqrt{\frac{B^{hl}}{B^{eq}}}, \tag{10}$$

based on conserved magnetic flux within the flux tube and assuming that the waves stay inside this flux tube. For the sake of simplicity, we assume a circular cross-section for $k_{\perp}$, since the wavenumbers vary over several orders of magnitude. Therefore, small differences in the perpendicular directions have no significant influence on the spectral ranges.

Considering that the wave frequency ω does not change along the field line, that is, $\omega_{eq} = \omega_{hl}$ using Equations 3 and 4, the parallel scale transforms according to:

$$k_{\parallel}^{hl} = \frac{\omega_{eq}}{v_{A,rel}^{hl}}\sqrt{1 + \left(k_{\perp}^{hl}\lambda_e^{hl}\right)^2} \tag{11}$$

$$= k_{\parallel}^{eq}\frac{v_{A,rel}^{eq}}{v_{A,rel}^{hl}}\sqrt{1 + \left(k_{\perp}^{eq}\right)^2 \cdot \left(\left(\rho_s^{eq}\right)^2 + \frac{3}{4}\left(\rho_i^{eq}\right)^2\right)}\sqrt{1 + \left(k_{\perp}^{hl}\lambda_e^{hl}\right)^2}. \tag{12}$$

As defined in the preceding section, the dipolar magnetic field strength and semi-relativistic Alfvén speed are denoted by B and $v_{A,rel} = \frac{v_A}{\sqrt{1+\left(\frac{v_A}{c}\right)^2}}$, respectively. The corresponding plasma length scales, that is, ion gyroradius, ion-acoustic gyroradius, and electron inertial length, are indicated by ρ_i, ρ_s, and λ_e.

For large perpendicular scales, that is, dispersionless MHD scales, the parallel mapping simplifies to

$$k_{\parallel}^{hl} = k_{\parallel}^{eq}\frac{v_{A,rel}^{eq}}{v_{A,rel}^{hl}}. \tag{13}$$

In Figure 2, we display how perpendicular scale and parallel scales of the turbulent fluctuations in the wing are related to the different turbulence models under consideration (Weak, strong and kinetic) and the different source locations where turbulence can be driven (in torus or outside the torus). In the left panel, we show the related scales at the respective turbulence generator regions. In the right panel, scales are shown mapped to the location of Juno's measurements in the high-latitudes. For the equatorial models, the largest parallel wavelength is $3.3\,R_J$ in the strong interaction strength of $\bar{\alpha} = 0.9$. As mentioned in Section 2, a weaker interaction strength results in a reduced convection time and hence in a smaller $\lambda_{\parallel}^{\max} = T_{conv}v_A^{eq}$. For a weak interaction strength in the limit of

$\bar{\alpha} = 0$, the parallel wavelengths are a factor of 10 smaller for all models. We show only the scales for the ρ_i-MHD breakdown scale as the λ_i-case are qualitatively similar (and identical up to the λ_i-MHD breakdown scale). The transition from MHD turbulence to ion-kinetic turbulence is visible as a change in the slope toward larger perpendicular wavenumbers.

The large-scale parallel wavelengths at their respective source locations (Figure 2 left) mapped to the high-latitudes (Figure 2 right) will result in even larger parallel wavelength as a result of increasing Alfvén speed (see Equation 13). In contrast, for the small scales, inertial effects counteract this increase based on decreasing perpendicular scale and lead to smaller parallel scales in the high-latitudes than at the respective source locations. This effect is strongest for the equatorial case and thus parallel wavelength based on equatorial turbulence can cover various orders of magnitude in the high-latitudes. However, it is very likely that large-scale waves will be partly reflected at the torus boundary due to a significant change in the Alfvén velocity (Hess et al., 2010). This will affect waves associated with a strong interaction strength $\bar{\alpha}$ more than for a lower one. The small-scale waves can leave the torus undamped (with respect to reflection) and propagate to the high-latitudes. These small-scale waves might undergo efficient wave-particle interaction and heat the observed ion and electron species toward high energies (Clark et al., 2020; Szalay, Bagenal, et al., 2020). The turbulence models with a source location outside the torus (see Figure 1) do not cover these small parallel scales, but instead account for even smaller perpendicular scales (because the local ρ_i-scale is smaller than at the equator), which is interesting for intense wave-particle interaction. Furthermore, waves with large parallel wavelength are generated by high-latitude turbulence, which were not present for the torus based models as a consequence of discussed reflection, and might explain the lowest observed frequencies of the power spectrum from Sulaiman et al. (2020).

We are now picking up on the idea from Section 2 and investigate the increased width of the IFPT achieved by Alfvén waves entering neighboring field lines during their propagation. In the dispersive regime, the group velocity of Alfvén waves develops a perpendicular component. For example, in the warm approximation for the Alfvén wave inside the torus (see Equation 3), the perpendicular group velocity is given by:

$$v_{gr}^{\perp} = \frac{\partial \omega}{\partial k_{\perp}} = \frac{k_{\parallel}}{k_{\perp}} \frac{k_{\perp}^2 \left(\rho_s^2 + \frac{3}{4}\rho_i^2\right)}{1 + k_{\perp}^2 \left(\rho_s^2 + \frac{3}{4}\rho_i^2\right)} v_{gr}^{\parallel}. \tag{14}$$

Again, $k_{\parallel}$ and $k_{\perp}$ describe the parallel and perpendicular wavenumber with respect to the local background magnetic field. As visible, the perpendicular component $v_{gr}^{\perp}$ is much smaller than the parallel one $\left(v_{gr}^{\parallel}\right)$ as a result of the anisotropic nature of small-scale Alfvén waves. Equivalent conclusions also hold for KAWs in the cold limit. Building on the idea of Borovsky (1993), we integrate $v_{gr}^{\perp}$ with respect to the travel time along the flux tube. We carry out our calculations for the equatorial ion gyroradius as smallest MHD perpendicular scale and the corresponding parallel scale is retrieved from the turbulence models introduced in Table 1. The models used for the mapping of $k_{\perp}$ and $k_{\parallel}$ along the field line to the high-latitudes are given by Equations 10 and 11. For a strong interaction strength of $\bar{\alpha} = 0.9$, we find swept perpendicular distances of 19 and 71 km for the weak and the strong MHD-turbulence model. For a weaker interaction strength $\bar{\alpha}$ this distance increases linearly with factor $(1 - \bar{\alpha})$. In the limit of $\bar{\alpha} = 0$, we obtain a factor 10 larger values, that is, 191 and 708 km for both turbulence models. To conclude, the IFPT or generally the MAW can be significantly extended in the high-latitudes by kinetic effects based on an equatorially located turbulence generator. The numbers suggest a larger interaction strength $\bar{\alpha}$ to be adequate for modeling.

5. Comparison of Doppler Shifted Frequency Contributions for Different Turbulence Models and Turbulence Generator Locations

In this section, we compare the frequency contributions of the derived Doppler shifted frequency expression from Equation 8 in the Juno spacecraft frame at the high-latitudes for turbulence generator regions inside and outside the torus. We consider the introduced Alfvénic turbulence models from Section 3. Here, we explicitly demonstrate that high-frequency time-variability due to turbulent Alfvén waves in the IFPT are not detectable within Juno measurements, but Doppler-shifted spatial structures still dominate the time-series observed by the Juno spacecraft. In the following, we present the results for the strong interaction strength of $\bar{\alpha} = 0.9$. The conclusions are fully equivalent for weak interaction strengths.

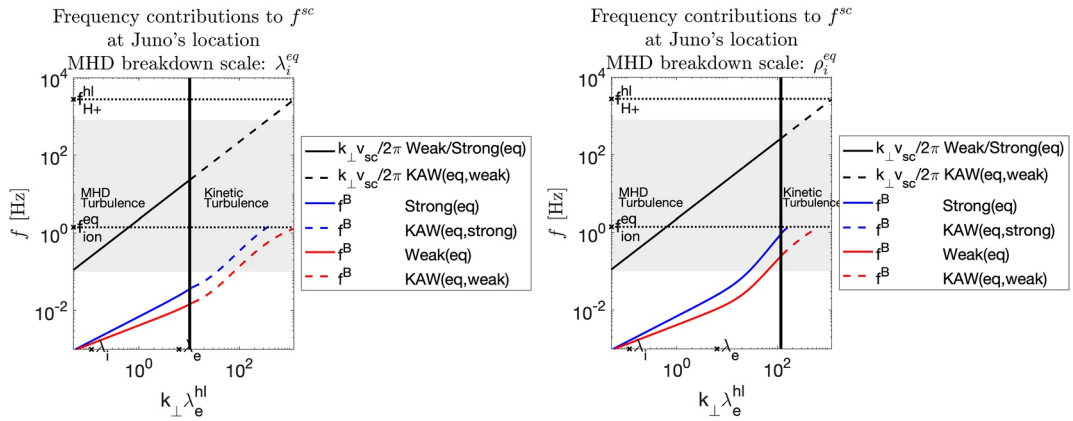

Figure 3. Doppler shifted frequencies (solid and dashed black lines) dominate over wave frequencies (blue and red lines) at the location of measurement calculated for a turbulence source location in the torus and various turbulence models. Left: contributions for λ_i^{eq} as MHD-breakdown scale, indicated by the vertical black line. Right: same for ρ_i^{eq}. The gray shaded region indicates the Juno-observed frequency range in the IFPT structure, $f = (0.1\text{–}800)$ Hz. The horizontal dotted lines indicate the ion cyclotron frequencies in the torus region (eq) and the location of measurement in the high-latitudes (hl). We consider a spacecraft speed of $v_{sc} = 51$ km/s according to Sulaiman et al. (2020).

5.1. Turbulence Produced in Torus and Propagated Into High-Latitudes

Beginning with the introduced perpendicular wavenumber spectral ranges in Section 4.2, we obtain the corresponding parallel wavenumbers from the turbulence relationships in Table 1 in the equatorial region. Proceeding from these sets of wavenumbers, we map them to the high-latitudes according to the mapping relations introduced in Section 4.2. We finally deduce the frequency contributions to the observable frequency in the spacecraft frame. These are the wave frequency in the plasma frame and the Doppler shifted contribution as shown in Equation 7. The wave frequencies are calculated by solving the dispersion relationship for the KAW from Lysak (2008). We use a routine from Schreiner and Saur (2017), which computes the wave frequency of the implicit dispersion relation via a Newton algorithm. The required plasma parameters used for its evaluation are based on the field line models from Su et al. (2006).

The resulting frequency contributions at the location of the Juno measurements are shown in Figure 3 for both MHD-breakdown scales $\left(\lambda_i^{eq}, \rho_i^{eq}\right)$, which are highlighted by the vertical black line in the plots. The solutions consider an interaction strength of $\bar{\alpha} = 0.9$. As visible from the wave frequency contributions, the Alfvén wave goes into resonance reaching the equatorial cyclotron frequency $f_{ion}^{eq} = \frac{\Omega_i^{eq}}{2\pi}$ as expected in the warm regime from theory. This sets the upper-frequency limit for temporal variations to be observable in the context of Alfvén waves. Thus, the investigation of Alfvénic turbulence located in the equatorial region (with $\omega^B < \Omega_i^{eq}$) automatically introduces an upper limit to temporal variations at high-latitudes via ω-conservation when applying the mapping relations from Equation 13 or Equation 11, respectively. Hence, although the cyclotron frequency of the protons at high-latitude Ω_i^{hl} is much larger than in the equatorial region due to the increase in magnetic field strength, the wave frequencies are still controlled by the equatorially generated frequencies.

The convective frequencies, that is, the Doppler-shifted perpendicular wavelength scales, are represented by the solid and dashed black lines in both plots of Figure 3. These dominate over the wave frequencies from the respective turbulence models assuming a strong interaction strength of $\bar{\alpha} = 0.9$. Even in the limit of zero interaction strength, that is, $\bar{\alpha} = 0$, the convective contributions still dominate the observable signal at the observed of the IFPT event regardless of the perpendicular spatial scale. These results are in accordance with the time scale comparisons from Section 2. This indicates that the magnetic fluctuation power spectrum from Sulaiman et al. (2020) needs to be interpreted with respect to the perpendicular wavenumber as $\omega^{sc} \simeq k_\perp v_B^{sc}$.

Now we turn to the question of which frequency range can be covered by Alfvén waves for the given setup. The MHD turbulence models (weak, strong) cover an observable frequency range of $f = [0.1, 262]$ Hz in the ρ_i^{eq}-MHD breakdown case (Figure 3 right). Above, the KAW turbulence convective frequency contributions cover the remaining part toward the 800 Hz from the observations which corresponds to a scale of $k_\perp \lambda_e^{hl} = 360$, that is,

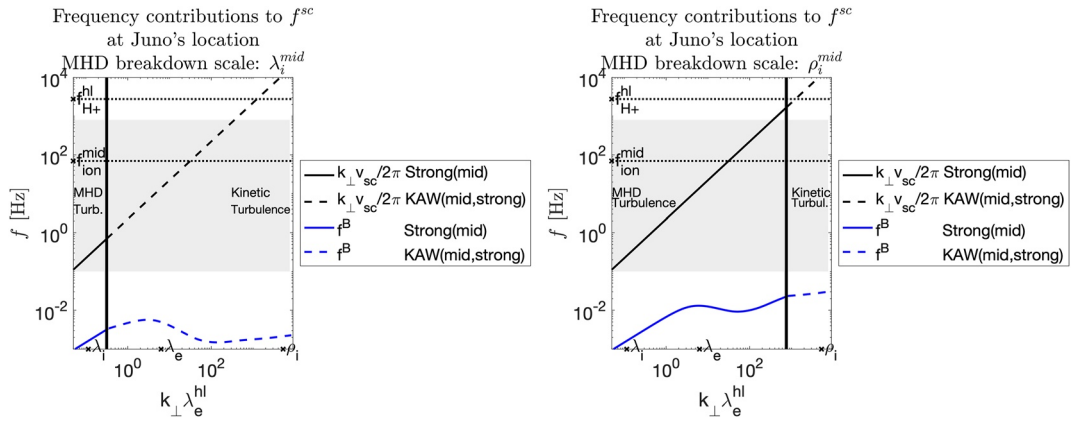

Figure 4. Doppler shifted frequencies (solid and dashed black lines) dominate over wave frequencies (blue lines) at the location of measurement calculated for a turbulence source location outside the torus at position mid (see Figure 1). Left: frequency contributions for a λ_i^{mid}-MHD breakdown; right: same for ρ_i^{mid} as MHD-breakdown scale. Labels are the same as for Figure 3.

$\lambda_\perp = \frac{2\pi}{k_\perp} = 6 \cdot 10^{-2}$ km. In the λ_i^{eq}-case, the KAW convective contributions cover a broader frequency range, that is, $f = [23, 800]$ Hz, as the ρ_i^{eq}-scale is much smaller than the λ_i^{eq}-scale. Both cases are associated with frequencies connected to the Waves instrument (above 50 Hz). However, it is unphysical that (kinetic) Alfvénic turbulence based on a ρ_i^{eq}-MHD breakdown scale originating in the torus can cover the whole frequency range in the high-latitudes. For small perpendicular scales, that is, the KAW range in Figure 3 (right), the Alfvén wave amplitude suffers from significant damping as its frequency reaches the cyclotron frequency. As a consequence, the propagating small-scale waves cannot reach the high-latitudes. By comparison, KAW turbulence as continuation of weak MHD turbulence is more plausible to cover a larger range of the observed frequencies than the strong MHD turbulence based KAW model, because the latter wave frequencies go into resonance at a larger perpendicular scale.

5.2. Turbulence Generated Outside the Torus Region

In the last section, we concluded that propagating small-scale equatorial Alfvén waves (KAWs) get damped on their way toward the high-latitudes and cannot account for larger frequencies of the observations (at least for a ρ_i^{eq}-MHD breakdown). However, filamented KAWs originating outside the torus can reach the location of measurement within a wave period. They survive the significant amplitude damping setting in at small spatial scales, that is, at the electron inertial length scale in the high-latitudes. Hence, we investigate KAW turbulence originating outside the torus as a promising candidate to explain the spectral slope of the observed magnetic power spectrum (see Section 6).

The frequency contributions based on turbulence originating from the mid-latitude position mapped to the location of measurement are shown in Figure 4. Similar to the equatorial based turbulence, Juno observes only convection frequencies, and thus, the wavefield would quasi-stationary convect past Juno. As a consequence, the observed power spectrum also needs to be interpreted with respect to the perpendicular wavenumber $k_\perp$. Equivalent conclusions can be drawn for high-latitude turbulence location, shown in Figure 5. The major difference to the equatorial discussed case is the significantly changed MHD-breakdown scale for ρ_i and λ_i as $\beta_i \ll 1$ due the stronger background magnetic field and the decreased plasma density toward higher latitudes. Analyzing the convective frequencies of both figures, we identify a frequency of $f_{sc} = 0.7$ Hz at the λ_i^{mid}-MHD breakdown scale (Figure 4) and $f_{sc} = 0.3$ Hz for the λ_i^{hl}-MHD breakdown scale (Figure 5). For the corresponding ρ_i-cases, these frequencies lie significantly above 800 Hz. In the $\lambda_i^{mid,hl}$-MHD breakdown cases, KAW turbulence would take up large parts of the observed power spectrum. Based on the lack of reliable density data along the IFT, parameters used in this study allow for some variability. Reduction of the number density by a factor of 7 is sufficient so that the ion inertial length scale corresponds to the largest perpendicular scale of the system in the high-latitude case. The mid-latitude case requires a density reduction by a factor of 60 for the same effect.

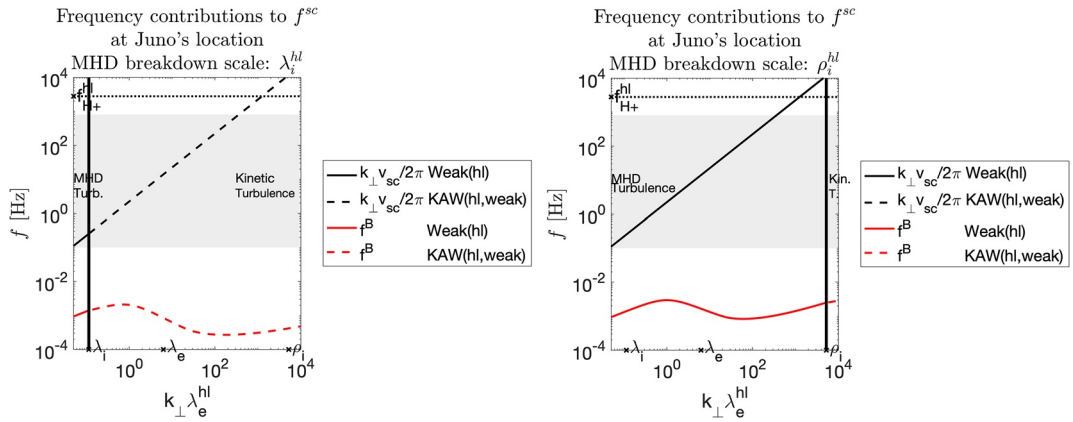

Figure 5. Wave (red lines) and Doppler (solid and dashed black lines) frequency contributions at the location of measurement based on turbulence source at the same location. Left: frequency contributions for λ_i^{hl}-MHD breakdown; right: same for ρ_i^{hl} as MHD-breakdown scale. Labels are the same as for Figure 3.

Consequently, KAW-turbulence would cover the frequency range by its own and no MHD turbulence would set up. In the $\rho_i^{mid,hl}$-cases, KAW turbulence would not play any role for the desired frequency range. As discussed in Section 4.2, an MHD-breakdown at the λ_i-scale seems to be reasonable in the high-latitudes. For the ρ_i-scale based MHD-breakdown, strong-MHD and weak-MHD turbulence cover the whole frequency range at the location of measurement for their respective generator locations. However, it is to be expected that Alfvén waves get significantly damped for observed frequencies above ∼50 Hz as they reach electron inertial length scales (Saur et al., 2018).

5.3. Curved Background Field and Wavevector Directions

In this work, we study properties of wave turbulence which develop and propagate in a curved background magnetic field. The curved magnetic field might lead to some uncertainty in the separation of turbulent wavefields into perpendicular and parallel components of the associated wavevectors with respect to the background magnetic field and might smear out anisotropies. Uncertainty about how to choose the appropriate background field which controls the wavevector orientation of a wave package also exists in the solar wind (e.g., Gerick et al., 2017). In case that the turbulence is controlled by the physics of critical balance (Goldreich & Sridhar, 1995), then a much larger fraction of the field-to-flow angles between 0° and 90°, represent a perpendicular cascade compared to a parallel cascade and thus magnetic field measurements in the solar wind for nearly all background magnetic field orientations represent a perpendicular cascade (e.g., Gerick et al., 2017; Horbury et al., 2008).

To understand the described wavevector phenomena it is additionally important to note that frequency measurements in a moving spacecraft do not relate one single wave vector to one single frequency, but an infinite number of wave vectors contribute to the power density at one frequency. This fact has been frequently pointed out in the literature (e.g., Fredricks & Coroniti, 1976; Howes et al., 2014; von Papen & Saur, 2015). It can be seen in Equation 5 that a manifold of wavevectors given by $\vec{k} \cdot \vec{v_{rel}} = \omega_{Doppler}$ contribute to one $\omega_{Doppler}$. In the following, we will discuss this effect to demonstrate that it further contributes to our hypothesis that Juno's frequency spectrum is dominated by perpendicular wave vectors $k_\perp$. In the previous analysis in Section 5 of this study, we had only related one frequency to one wavevector for simplicity.

In Figure 6, we show the energy populated scales in k-space associated with the turbulent wavefield at high-latitudes (blue area). We assumed a KAW turbulent cascade with a critical balance wavenumber relation from Table 1, which basically populates the k-space below the critical balance boundary (blue-dashed line). For simplicity of the representation, we display power contributions only exactly below the critical balance boundary. The power distribution around the critical balance boundary is discussed in the literature as falling off exponentially above it or it is even often assumed to be non-existent at all above the boundary (see discussion in von Papen & Saur, 2015). The colored solid lines show the contours in k-space which contributes to individual frequencies

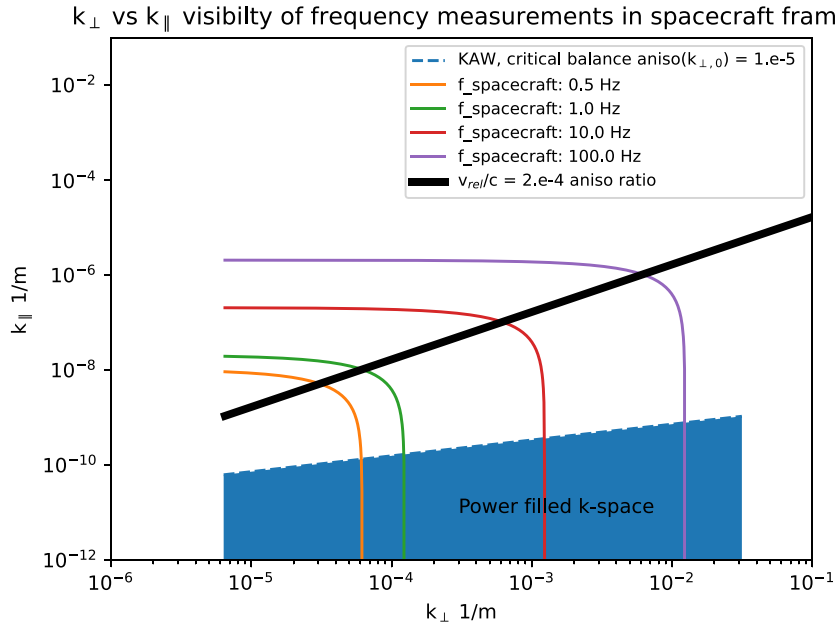

Figure 6. Power populated k-space (blue area) at high-latitudes scanned by Juno at different spacecraft frequencies under the assumption of a critically balanced spectrum (colored solid lines). The black solid line represents the transition boundary from a $k_{\parallel}$- toward a $k_{\perp}$-scanning of the turbulent wavefield.

observed by Juno between [0.5–100] Hz. Expressing ω^B in Equation 7 with $v_A^{rel} k_{\parallel} \approx c\, k_{\parallel}$, the contours in k-space associate with observable spacecraft frequency f_{sc} are determined by:

$$k_{\perp} \sin(\theta) = \frac{2\pi f_{sc}}{v} - k_{\parallel} \cos(\theta). \tag{15}$$

Here, $\sin(\theta) = \frac{v_{sc}^B}{v_A^{rel}} \approx \frac{v_{sc}^B}{c}$ defines the field-to-flow angle in dependence of the Alfvén speed v_A^{rel} and the spacecraft velocity relative to the plasma frame v_{sc}^B. When the contours cut primarily along $k_{\parallel}$ through the region of k-space populated with power, then the frequency spectrum represents a $k_{\perp}$ spectrum and vice versa. In Figure 6, the contours cut along $k_{\parallel}$ in the dark blue region and thus different spacecraft frequencies correspond to different $k_{\perp}$. The thick solid black line indicates the transition of a primarily $k_{\parallel}$-based scanning of the wavefield toward a $k_{\perp}$-based scanning, which is described by $k_{\parallel} = v_{sc}^B / v_A^{rel} \cdot k_{\perp}$ and related anisotropy ratio of $v_{sc}^B / v_A^{rel} = 2 \cdot 10^{-4}$. As visible, power is only populated significantly below the transition boundary because the turbulent cascade under consideration is driven to large anisotropies on the order of 10^{-6} or smaller. Therefore, the anisotropy of turbulence can be smeared out by at least 1–2 orders of magnitude due to the possible effects of a curved background magnetic field and still represent a $k_{\perp}$ spectrum.

The model applied here stems from models which assume that the separation of $k_{\perp}$ and $k_{\parallel}$ is universal in three-dimensional space, that is, they assume a homogeneous background magnetic field $\vec{B}_0$ exists, which allows a separation of wave vectors in direction parallel and perpendicular to this field. In Jupiter's magnetosphere, the background magnetic field is not homogeneous. It is Jupiter's internal magnetic field $\vec{B}_J(\vec{x})$, which is to first order a dipole magnetic field above Jupiter's surface. The curvature of $\vec{B}_J$ raises the question what is locally the physically adequate orientation that organizes wave vector space and how much uncertainty lies in the separation of $k_{\perp}$ and $k_{\parallel}$ in our model. In our estimates, we assume that the tangent direction to the background field $\vec{B}_J$ at the location of the Juno measurements determines the separation.

An alternative view for the uncertainty would be, for example, to calculate the averaged background magnetic field $< \vec{B}_J >$ over one wavelength along $\vec{B}_J$ and compare the averaged background field with the local $\vec{B}_J(\vec{x})$ along this distance. For a wavelength of 1 R_J, which corresponds to roughly $k_{\parallel} = 10^{-6}\ \mathrm{m}^{-1}$, the angular deviations between local background field and averaged background field are on the order 0.1–0.01 radians. If this is used as an estimate for the uncertainty in the separation of $k_{\perp}$ and $k_{\parallel}$, it would lead to an uncertainty of the same order of

0.1–0.01. A wavelength a factor of 10 smaller will reduce the uncertainty by a factor of 10 as well. These uncertainties, however, would be larger than the required anisotropy ratio of 2×10^{-4} and thus a useful separation in $k_\perp$ and $k_\parallel$ to determine if the spectrum is a Doppler-shifted $k_\perp$ spectrum as compared to a time-variable spectrum due to parallel propagating waves would not be possible.

The local approach of this work assumes that $k_\perp$ is determined by the direction locally perpendicular to the background field $\vec{B}_J$. Because perpendicular scales are expected to develop up to $k_\perp = 10^{-2}$ m^{-1} corresponding to very small physical scales on the order of 10^{-4} R_J, the associated direction perpendicular to the background field is much less uncertain (less than 10^{-4}). We note that the resulting wave packages (or eddies) are extremely elongated structures. These wave packages lie and propagate along the curved background field. The parallel wave length of such a structure is thus approximately given by the length of the wave package (or turbulent eddy) along the curved background magnetic and we do not expect it to be controlled by an average $< \vec{B}_J >$ due to the slimness of the wave packages. Therefore we expect that the magnetic field time-series obtained by Juno during Io's footprint tail crossing represents measurements of a $k_\perp$ turbulent cascade and that explicit temporal variations of turbulent Alfvén waves are not expected to be observable by Juno in the high-latitudes at the frequency ranges analyzed here. The possible consequences for the turbulence models will be discussed in the next section.

It is important to stress that turbulent spectral evolution along curved, very large amplitude background magnetic fields is not sufficiently studied to the authors' knowledge. This leaves a basic uncertainty in our interpretation of the observed magnetic field fluctuations.

6. Comparison of Theoretical and Observed Turbulent Magnetic Power Spectra in the High-Latitudes

Based on our modeling studies from Section 5, we propose that the observed frequencies in the spacecraft frame are due to Doppler shifted perpendicular wavenumbers. This is contrary to the assumption of Gershman et al. (2019) and Sulaiman et al. (2020), who considered a relationship of the form $\omega^{sc} = k_\parallel v_A^{rel}$. Due to the anisotropic nature of filamentation of the considered magnetic turbulence models, energy cascades in perpendicular and parallel direction with different spectral indices. Consequently, the interpretation of the observed power spectral index changes with respect to the potential turbulence mechanism at work. In the following, we fit selected turbulence models to the observed power spectral density in the form of:

$$P(f) = P_0 \left(\frac{f}{f_0} \right)^\alpha \tag{16}$$

where f is the frequency in the spacecraft frame, $P_0 = P(f_0)$ describes the power spectral density at the minimal frequency f_0 and α denotes the spectral index. We choose $f_0 = 0.2$ Hz for the analysis to avoid effects from leakage and aliasing in accordance with the choice of Sulaiman et al. (2020).

Assuming that the non-overlapping MAG and Waves spectra are the result of a single cascading process in the inertial turbulence regime ($f = [0.2, 800]$ Hz), Sulaiman et al. (2020) fit a spectral slope of $\alpha = -2.35 \pm 0.07$. However, the data fit allows for variability in the spectral slope, when considering only restricted frequency ranges and thus assuming a spectral break in the observed spectrum. Fitting only the MAG data ($f = [0.2, 3]$ Hz) results in $\alpha = -2.96 \pm 0.22$ and for the Waves data ($f = [50, 800]$ Hz) even in $\alpha = -3.51 \pm 0.36$. Both values for α are not considered here. Instead, we choose selected turbulence models from our analysis in Section 5 for comparison with the data involving both instruments frequency ranges.

The model turbulence power spectra in Figure 7 display a least squares fits with their fixed spectral index (but variable P_0) to the respective data fit in logarithmic space. From the equatorial models (Figure 7 left), we show the strong MHD turbulence ($\alpha = -5/3$) and weak ($\alpha = -2$) MHD-ρ_i^{eq} turbulence models (see definition for MHD-ρ_i^{eq} in Section 4.2), which cover a frequency range of $f = [0.2, 262]$ Hz. The corresponding data fit (green line) has a spectral index of $\alpha = -2.23 \pm 0.08$. From visual comparison, it is obvious that equatorial Weak turbulence suits the data fit better than the strong GS model, because a -2 slope fits better to a -2.23 slope than $-5/3$.

For the turbulence source locations outside the Io torus, fitted power spectra are shown for the weak MHD-ρ_i^{hl} and the KAW-λ_i^{mid} models in Figure 7 (right). As presented for the equatorial source location, strong turbulence in the

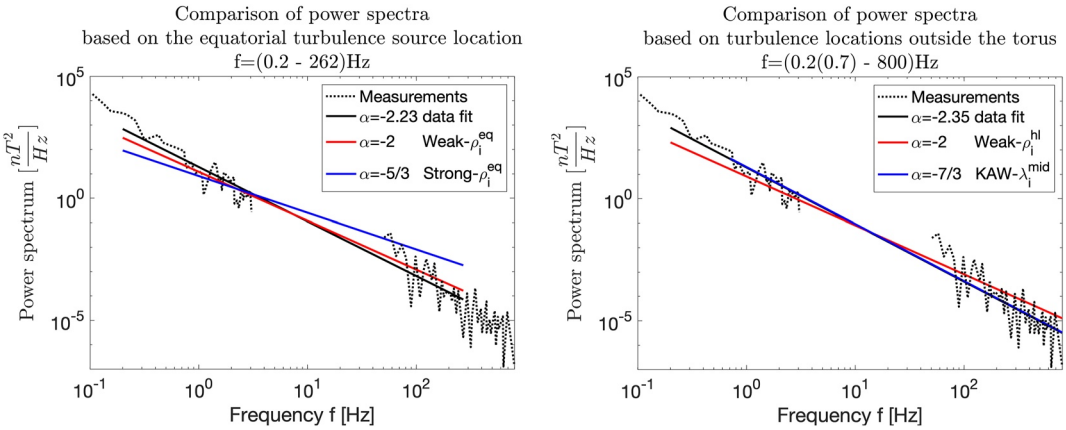

Figure 7. Power spectral density of the magnetic fluctuations from MAG and Waves data (black dotted lines) displayed together with fits to the data and the indicated turbulence models. Left: fit with equatorial MHD turbulence models (ρ_i^{eq}-breakdown) in a frequency-range of $f = [0.2, 262]$ Hz. Right: fit with high-latitude turbulence models weak-ρ_i^{hl} and KAW-λ_i^{mid} in the frequency range $f = [0.2(0.7), 800]$ Hz according to the analysis of the turbulence frequencies. The minimal frequencies $f = 0.2$ Hz and $f = 0.7$ Hz refer to the weak-ρ_i^{hl} and KAW-λ_i^{mid} cases, respectively. The least squares fitted lines (black solid lines) consider only the frequency ranges where the turbulent models apply.

mid latitudes also does not fit the data well and will be not considered here. While the weak turbulence model covers the whole frequency range, the KAW-range is restricted to $f = [0.7, 800]$ Hz. The corresponding data fits exhibit an $\alpha = -2.35 \pm 0.07$ slope and an $\alpha = -2.31 \pm 0.08$ slope, respectively. The high-latitude Weak and the mid-latitude based KAW spectra fit the data fairly well. Especially, the KAW spectral index is fully consistent within the error bars of the fitted spectrum with values of $-7/3$ and -2.31 ± 0.08, respectively. A comparable conclusion can be also drawn the KAW-λ_i^{hl} model, which is not shown here.

We note that the ion-cyclotron frequency lies at larger than 4,400 Hz during the Io flyby (Sulaiman et al., 2020). The ion-cyclotron frequency is not Doppler-shifted, but is seen in the spacecraft frame at approximately the same frequency. Ion cyclotron wave near the ion cyclotron frequency are characterized by $k_{\|} \to \infty$ and propagation angle $\Theta = 0°$ (Stix, 1992; Sulaiman et al., 2020), which is consistent with the none Doppler-shifted ion cyclotron frequency. The ion cyclotron frequency lies well above the frequency range of the turbulence cascades discussed here and both processes do not appear to be directly linked.

Comparing theoretical and observed averaged wave amplitudes gives further insight into the physics. Here, we only discuss the data fit of the whole frequency range, that is, $f = [0.2, 800]$ Hz. From integration of the associated power spectrum over this frequency range, we come up with an average fluctuation amplitude of $\delta B = 12$ nT. Considering even smaller frequencies down to 0.1 Hz, we obtain $\delta B = 21$ nT. We can derive a theoretical model for the fluctuation amplitude, accounting only for geometric changes based on the converging magnetic field topology and conserved total wave power within a flux tube. We can express the resulting fluctuation amplitude in the high-latitudes as:

$$\delta B^{hl} = \delta B^{Io} \sqrt{\frac{B^{hl}}{B^{eq}} \frac{v_{A,rel}^{eq}}{v_{A,rel}^{hl}}}, \tag{17}$$

where $v_{A,rel}$ and B denotes the semi-relativistic Alfvén speed and the magnetic field strength at the equator and in the high-latitudes. Using an Io-related maximal fluctuation amplitude of $\delta B^{Io} = 400$ nT, we can calculate the resulting fluctuation in the high-latitudes to $\delta B^{hl} = 148$ nT. This amplitude is significantly larger than the observed one. This is a hint that further physical processes occur in the system such as wave reflection and dissipation due to wave-particle interaction. Consequently, the Alfvén wave amplitude decreases during propagation. However, we also point out that calculation of theoretical turbulent Poynting fluxes requires a more sophisticated model for the fluctuation amplitude, which is outside the scope of this paper. We forgo an exact calculation of the involved integrated power fluxes for the different turbulence models as these sensitively depend on the smallest frequency of concern because the energy input scales contain most power. This complicates a fair comparison for

different frequency ranges. Furthermore, we restricted our analysis to frequencies larger than $f = 0.2$ Hz to avoid effects from numerical issues.

We like to end our discussion with an evaluation of the energy cascade flux and thus of the heating efficiency for the weak and the KAW turbulence. The weak turbulent heating rate (Galtier et al., 2000; Ng & Bhattacharjee, 1997; Saur, 2004) is given by

$$q_{turb}^{weak} = \frac{1}{\sqrt{\mu_0^3 \rho}} \frac{\delta B^4}{B_0} \frac{l_\parallel}{l_\perp^2} \tag{18}$$

in units of W/m^3. Using $l_\parallel = \lambda_\parallel^{\max} = 3.3\, R_J$ in case of $\bar{\alpha} = 0.9$, $l_\perp = \lambda_\perp^{\max} = 3.6 R_{Io}$, $\rho = 4.3 \times 10^{-17}$ kg/m^3, $B_0 = 2{,}000$ nT and $\delta B = 400$ nT as estimates for an equatorial turbulence source location, we find $q_{turb}^{weak} = 7.4 \cdot 10^{-9}$ W/m^3. From integration of this energy flux density over the flux tube volume up to the torus boundary, we can estimate the turbulence heating power to 4.2×10^{13}W. Note, this is the cascade rate of the turbulence to smaller scales. It does not necessarily mean the energy is dissipated within the torus, but when in particular the small-scale fluctuations of this cascade are transmitted through the torus boundaries, the dissipation can occur at high-latitudes. This value proves the efficiency of weak turbulence to transfer sufficient energy toward the particles and finally account for the observed emissions in infrared and UV. Their corresponding electron input energies are on the order of 10^9–10^{11}W (Saur et al., 2013). A similar estimate can be provided for KAW turbulence using

$$q_{turb}^{KAW} = \frac{\delta B^3}{\sqrt{\mu_0^3 \rho}} \frac{\lambda_i}{l_\perp^2}, \tag{19}$$

which is an adapted version from von Papen et al. (2014) for the ion inertial length λ_i. Applying this formula to a turbulence source location at mid-latitudes using $l_\perp = \lambda_i^{mid} = 332$ km, $\rho = 10^{-20}$ kg/m^3 and $\delta B^{mid} = 50$ nT, we find $q_{turb}^{KAW} = 2.7 \cdot 10^{-9}$ W/m^3. Integrating q_{turb}^{KAW} over the flux tube volume outside the torus boundary results in a dissipation rate of 7.2×10^{12} W. To conclude, weak MHD as well as sub-ion KAW turbulence are associated with significant energy cascades and thus dissipation rates, which is an indication that turbulence is indeed a realistic mechanism to transfer energy from large-scale magnetic field perturbations into the charged particles and finally account for the observation of the Io footprint and IFPT phenomena. In particular, estimation of instantaneous Poynting fluxes for the discussed weak MHD and kinetic turbulence cases gives values of 1.9 and 1.0 W/m^2, respectively. These underpin the heating potential compared to the observed JADE electron energy flux density of 580 mW/m^2 (Szalay, Allegrini, et al., 2020).

We show that weak-MHD turbulence in the torus or KAW turbulence developed outside the Io torus are reasonable mechanisms for the observed spectrum. Strong-MHD turbulence is not a likely candidate to explain the power spectrum. We cannot clearly exclude models based on their associated power or MHD-breakdown scale. This is also caused by the MAG and Waves data gap between $f = [5, 50]$ Hz. Hence, predictions regarding spectral breaks are difficult to assess. For example, the Weak-λ_i^{eq} model with a frequency range of $f = [0.2, 28]$ Hz from Section 5.1 cannot be satisfyingly constrained by the data and introduces a uncertainty in the interpretation. Model fittings considering only the MAG data in the low-frequency range will give non-satisfying results regarding the investigated turbulence models with the steep slope of $\alpha = -2.96 \pm 0.22$ as mentioned in the beginning of this section. However, observations in Jupiter's and Saturn's equatorial region show that low-frequency turbulence is not fully stationary and might not be fully developed all the time, which results in a time-variable spectral slope at low frequencies (Saur, 2021; Tao et al., 2015; von Papen et al., 2014). Therefore the low-frequency part of the spectrum of the IFT at high-latitudes might be variable as well. This needs to be investigated by analysis of further IFT and tail crossings.

7. Conclusion

Recent analysis of MAG and Waves instrument data obtained during Juno's PJ12 IFPT crossing at low-altitude (Sulaiman et al., 2020) revealed a power law-like power spectrum in the magnetic field fluctuations. Such behavior is characteristic for energy cascading phenomena toward smaller spatial and temporal scales by turbulent

processes. Thus, in this work, we investigate the idea of Alfvénic turbulence to drive the energetics in the IFT. Due to Io's interaction with the surrounding plasma, Alfvén waves are generated which propagate along the magnetic field lines toward the high-latitude region. In the Io-fixed frame, these waves are stationary for the lowest frequencies corresponding to spatial scales of the size of Io. The formed Alfvén wings are essential for the energy transport to the high-latitudes in both hemispheres. As a result of the complex interaction of Io with the torus plasma and also from reflection processes at ionosphere and torus boundary, filamentation processes can occur anywhere along the flux tube and set up a turbulent cascade. We describe these filamentary fluctuations in terms of KAWs. On spatial and temporal scales comparable to particle scales they can finally undergo efficient wave-particle interaction and account for observed strong particle fluxes.

We use observed frequencies, IFPT crossing time, and the power spectral index to characterize the spatio-temporal wavefield and involved turbulent processes. Based on estimations of relevant propagation and interaction time scales associated with turbulence, we consider strong and weak turbulent processes with generator locations in and also outside the torus.

Examination of the wave and Doppler shifted frequency contributions to the observed spacecraft low-frequency range indicates that the magnetic fluctuation power spectrum from Sulaiman et al. (2020) needs to be interpreted with respect to the perpendicular wavenumber regardless of the turbulence model and source location considered. Consequently, we reinterpret the spectral index and investigate power spectral fittings to the observed data. We conclude that equatorial strong MHD turbulence is not expected to be present in the high-latitudes as a consequence of the low spectral index, contrary to the suggestion of Gershman et al. (2019) and Sulaiman et al. (2020). Instead, we expect KAWs as a result of KAW turbulence outside the torus with an MHD-breakdown scale at the ion inertial length to be present at the location of measurement. Weak MHD turbulence with a smallest perpendicular scale matching the equatorial ion gyroradius at the source location is a further interesting candidate to explain the observed magnetic power spectrum. Calculation of the corresponding dissipation rates for both models support the idea of turbulence to be responsible for the transport of wave energy to small scales such that wave-particle interaction can energize particles observed in the IFPT.

Our analysis is sensitive to assumed model parameters used in this study. Especially the density and the magnetic field strength have significant influence on the plasma length scales and hence on the mapping relations and involved frequencies for the turbulence models. However, even with the assumption of a dipolar magnetic field, higher-order moments from the dynamo field are found to significantly contribute only closer to Jupiter than the IFPT crossing (Connerney et al., 2018).

Additionally, temporal variability of the parameters owing to Io's position within the torus and unknown dynamic processes introduces a further complexity to the system. For instance, temporal and spatial variability of the spectral index is observed in the equatorial region (Chust et al., 2005) and complicates strong conclusions on the acting turbulence mechanism in the IFPT. The wavefield at Io is anisotropic at largest scales as a consequence of different time scales of wave propagation and plasma convection. We account for this anisotropy behavior with the usage of anisotropy factors in the turbulence models. Physical interpretation of the high-latitude data as result of mixed states of turbulence (influencing the spectral index) or a non-fully developed state of the cascade (which restricts the frequency range of the turbulent waves) is not fully accessible with the given Juno data basis. We interpret at least the lower regime of the observed frequencies in the IFPT to originate from Alfvénic turbulence.

We point out that further studies are needed to investigate the evolution of turbulent fluctuations in bounded systems, such as the Jupiter system or the IFT which is limited within the boundaries of Jupiter's magnetosphere and its ionospheres (see also discussion in Saur (2021)). In particular, we like to highlight the fact that currently available turbulence theories in the literature such as applied in the context of this paper consider Cartesian geometries in infinitely extended media with constant background magnetic fields. To the authors' knowledge, similar studies for curved background fields are missing. Future basic studies on the evolution of turbulent wavefields in magnetospheric environments with curved background magnetic fields are required. Of particular importance of such studies should be the investigation of anisotropic properties in turbulent cascades including the correct anisotropy frame, which is even debated in solar wind turbulence with apparently simpler geometries (see discussion in Gerick et al., 2017 or Oughton & Matthaeus, 2020). The uncertainty in the description and evolution of anisotropy introduce however also a basic uncertainty in our interpretation of wavevector association of the magnetic field fluctuations by Juno.

Based on wave amplitude damping arguments at scales smaller than electron inertial length in the high-latitudes, it is conceivable that another wave mode covers the upper end of the considered frequency range. Sulaiman et al. (2020) suggest the ion-cyclotron mode as a reasonable candidate. Further studies and observations of the IFT are required to tackle these questions and will remain for future research. In this work, we took the first systematic step to unravel the substructure of the IFT and the IFPT.

Data Availability Statement

The MAG and Waves data used to generate the power spectral data are presented in Sulaiman et al. (2020). Their corresponding data IDs are JNO-J-3-FGM-CAL-V1.0 (https://doi.org/10.17189/1519711) and JNO-E/J/SS-WAV-3-CDR-BSTFULL-V2.0 (https://doi.org/10.17189/1522461). The file for the MAG data file is named `fgm_jno_l3_2018091pc_pj12_v02.sts`. This is in pc (planetocentric) coordinate system at the highest cadence, that is, 64 vectors/s. The waves data file is named `WAV_2018091T113117_B_BIN_V02.DAT`. This is the burst mode for the magnetic search coil data.

Acknowledgments
S. Janser and J. Saur acknowledge funding by the Deutsche Forschungsgemeinschaft under Grant SA 1772/6-1. Open Access funding enabled and organized by Projekt DEAL.

References

Acuna, M. H., Neubauer, F. M., & Ness, N. F. (1981). Standing Alfvén wave current system at Io: Voyager 1 observations. *Journal of Geophysical Research*, *86*(A10), 8513–8521. https://doi.org/10.1029/JA086iA10p08513

Belcher, J. W., Goertz, C. K., Sullivan, J. D., & Acuna, M. H. (1981). Plasma observations of the Alvén wave generated by Io. *Journal of Geophysical Research*, *86*(A10), 8508–8512. https://doi.org/10.1029/JA086iA10p08508

Bigg, E. K. (1964). Influence of the satellite Io on Jupiter's decametric emission. *Nature*, *203*(4949), 1008–1010. https://doi.org/10.1038/2031008a0

Blöcker, A., Saur, J., Roth, L., & Strobel, D. F. (2018). MHD modeling of the plasma interaction with Io's asymmetric atmosphere. *Journal of Geophysical Research: Space Physics*, *123*(11), 9286–9311. https://doi.org/10.1029/2018JA025747

Bonfond, B., Grodent, D., Gérard, J. C., Radioti, A., Saur, J., & Jacobsen, S. (2008). UV Io footprint leading spot: A key feature for understanding the UV Io footprint multiplicity? *Geophysical Research Letters*, *35*(5), L05107. https://doi.org/10.1029/2007GL032418

Bonfond, B., Saur, J., Grodent, D., Badman, S. V., Bisikalo, D., Shematovich, V., et al. (2017). The tails of the satellite auroral footprints at Jupiter. *Journal of Geophysical Research: Space Physics*, *122*(8), 7985–7996. https://doi.org/10.1002/2017JA024370

Borovsky, J. E. (1993). Auroral arc thicknesses as predicted by various theories. *Journal of Geophysical Research*, *98*(A4), 6101–6138. https://doi.org/10.1029/92JA02242

Broadfoot, A. L., Belton, M. J. S., Takacs, P. Z., Sandel, B. R., Shemansky, D. E., Holberg, J. B., et al. (1979). Extreme ultraviolet observations from Voyager 1 encounter with Jupiter. *Science*, *204*(4396), 979–982. https://doi.org/10.1126/science.204.4396.979

Chen, C. H. K., Leung, L., Boldyrev, S., Maruca, B. A., & Bale, S. D. (2014). Ion-scale spectral break of solar wind turbulence at high and low beta. *Geophysical Research Letters*, *41*(22), 8081–8088. https://doi.org/10.1002/2014GL062009

Chust, T., Roux, A., Kurth, W. S., Gurnett, D. A., Kivelson, M. G., & Khurana, K. K. (2005). Are Io's Alfvén wings filamented? Galileo observations. *Planetary and Space Science*, *53*(4), 395–412. https://doi.org/10.1016/j.pss.2004.09.021

Clark, G., Mauk, B. H., Kollmann, P., Szalay, J. R., Sulaiman, A. H., Gershman, D. J., et al. (2020). Energetic proton acceleration associated with Io's footprint tail. *Geophysical Research Letters*, *47*(24), e90839. https://doi.org/10.1029/2020GL090839

Clarke, J. T., Ballester, G. E., Trauger, J., Evans, R., Connerney, J. E. P., Stapelfeldt, K., et al. (1996). Far-ultraviolet imaging of Jupiter's aurora and the lo "footprint". *Science*, *274*(5286), 404–409. https://doi.org/10.1126/science.274.5286.404

Connerney, J. E. P., Baron, R., Satoh, T., & Owen, T. (1993). Images of excited H_3^+ at the foot of the Io flux tube in Jupiter's atmosphere. *Science*, *262*(5136), 1035–1038. https://doi.org/10.1126/science.262.5136.1035

Connerney, J. E. P., Benn, M., Bjarno, J. B., Denver, T., Espley, J., Jorgensen, J. L., et al. (2017). The Juno magnetic field investigation. *Space Science Reviews*, *213*(1–4), 39–138. https://doi.org/10.1007/s11214-017-0334-z

Connerney, J. E. P., Kotsiaros, S., Oliversen, R. J., Espley, J. R., Joergensen, J. L., Joergensen, P. S., et al. (2018). A new model of Jupiter's magnetic field from Juno's first nine orbits. *Geophysical Research Letters*, *45*(6), 2590–2596. https://doi.org/10.1002/2018GL077312

Connerney, J. E. P., & Satoh, T. (2000). The H_3^+ ion: A remote diagnostic of the Jovian magnetosphere. *Astronomy, Physics, and Chemistry of H3+*, *358*(1774), 2359–2483. https://doi.org/10.1098/rsta.2000.0661

Crary, F. J. (1997). On the generation of an electron beam by Io. *Journal of Geophysical Research*, *102*(A1), 37–49. https://doi.org/10.1029/96JA02409

Crary, F. J., & Bagenal, F. (1997). Coupling the plasma interaction at Io to Jupiter. *Geophysical Research Letters*, *24*(17), 2135–2138. https://doi.org/10.1029/97GL02248

Damiano, P. A., Delamere, P. A., Stauffer, B., Ng, C. S., & Johnson, J. R. (2019). Kinetic simulations of electron acceleration by dispersive scale Alfvén waves in Jupiter's magnetosphere. *Geophysical Research Letters*, *46*(6), 3043–3051. https://doi.org/10.1029/2018GL081219

Das, A. C., & Ip, W. H. (1992). Particle acceleration by kinetic Alfvén waves in the Io plasma torus. *Planetary and Space Science*, *40*(11), 1499–1502. https://doi.org/10.1016/0032-0633(92)90046-Q

Delamere, P. A., Bagenal, F., Ergun, R., & Su, Y. J. (2003). Momentum transfer between the Io plasma wake and Jupiter's ionosphere. *Journal of Geophysical Research: Space Physics*, *108*(A6), 1241. https://doi.org/10.1029/2002JA009530

Franci, L., Landi, S., Matteini, L., Verdini, A., & Hellinger, P. (2016). Plasma beta dependence of the ion-scale spectral break of solar wind turbulence: High-resolution 2D hybrid simulations. *The Astrophysical Journal*, *833*(1), 91. https://doi.org/10.3847/1538-4357/833/1/91

Fredricks, R. W., & Coroniti, F. V. (1976). Ambiguities in the deduction of rest frame fluctuation spectrums from spectrums computed in moving frames. *Journal of Geophysical Research*, *81*(A31), 5591–5595. https://doi.org/10.1029/JA081i031p05591

Frisch, U. (1995). *Turbulence: The legacy of an Kolmogorov*. Cambridge University Press.

Galtier, S., Nazarenko, S. V., Newell, A. C., & Pouquet, A. (2000). A weak turbulence theory for incompressible magnetohydrodynamics. *Journal of Plasma Physics*, *63*(5), 447–488. https://doi.org/10.1017/S0022377899008284

Gerick, F., Saur, J., & von Papen, M. (2017). The uncertainty of local background magnetic field orientation in anisotropic plasma turbulence. *The Astrophysical Journal*, *843*(1), 5. https://doi.org/10.3847/1538-4357/aa767c

Gershman, D. J., Connerney, J. E. P., Kotsiaros, S., DiBraccio, G. A., Martos, Y. M., Viñas, A. F., et al. (2019). Alfvénic fluctuations associated with Jupiter's auroral emissions. *Geophysical Research Letters*, *46*(13), 7157–7165. https://doi.org/10.1029/2019GL082951

Goldreich, P., & Lynden-Bell, D. (1969). Io, a Jovian unipolar inductor. *Astrophysical Journal*, *156*, 59–78. https://doi.org/10.1086/149947

Goldreich, P., & Sridhar, S. (1995). Toward a theory of interstellar turbulence. II. Strong Alfvénic turbulence. *The Astrophysical Journal*, *438*, 763. https://doi.org/10.1086/175121

Hess, S. L. G., Delamere, P., Dols, V., Bonfond, B., & Swift, D. (2010). Power transmission and particle acceleration along the Io flux tube. *Journal of Geophysical Research: Space Physics*, *115*(A6), A06205. https://doi.org/10.1029/2009JA014928

Hill, T. W., & Vasyliūnas, V. M. (2002). Jovian auroral signature of Io's corotational wake. *Journal of Geophysical Research: Space Physics*, *107*(A12), SMP27-1–SMP27-5. https://doi.org/10.1029/2002JA009514

Horbury, T. S., Forman, M., & Oughton, S. (2008). Anisotropic scaling of magnetohydrodynamic turbulence. *Physical Review Letters*, *101*(17), 175005. https://doi.org/10.1103/PhysRevLett.101.175005

Howes, G. G., Cowley, S. C., Dorland, W., Hammett, G. W., Quataert, E., & Schekochihin, A. A. (2008). A model of turbulence in magnetized plasmas: Implications for the dissipation range in the solar wind. *Journal of Geophysical Research: Space Physics*, *113*(A5), A05103. https://doi.org/10.1029/2007JA012665

Howes, G. G., Klein, K. G., & TenBarge, J. M. (2014). Validity of the Taylor hypothesis for linear kinetic waves in the weakly collisional solar wind. *The Astrophysical Journal*, *789*(2), 106. https://doi.org/10.1088/0004-637X/789/2/106

Jacobsen, S., Neubauer, F. M., Saur, J., & Schilling, N. (2007). Io's nonlinear MHD-wavefield in the heterogeneous Jovian magnetosphere. *Geophysical Research Letters*, *34*(10), L10202. https://doi.org/10.1029/2006GL029187

Jones, S. T., & Su, Y. J. (2008). Role of dispersive Alfvén waves in generating parallel electric fields along the Io-Jupiter fluxtube. *Journal of Geophysical Research: Space Physics*, *113*(A12), A12205. https://doi.org/10.1029/2008JA013512

Kivelson, M. G., Bagenal, F., Kurth, W. S., Neubauer, F. M., Paranicas, C., & Saur, J. (2007). Magnetospheric interactions with satellites. In *Jupiter: The planet, satellites, and magnetosphere*. Cambridge University Press.

Kivelson, M. G., Khurana, K. K., Walker, R. J., Warnecke, J., Russell, C. T., Linker, J. A., et al. (1996). Io's interaction with the plasma torus: Galileo magnetometer report. *Science*, *274*(5286), 396–398. https://doi.org/10.1126/science.274.5286.396

Kurth, W. S., Hospodarsky, G. B., Kirchner, D. L., Mokrzycki, B. T., Averkamp, T. F., Robison, W. T., et al. (2017). The Juno waves investigation. *Space Science Reviews*, *213*(1–4), 347–392. https://doi.org/10.1007/s11214-017-0396-y

Lysak, R. L. (2008). On the dispersion relation for the kinetic Alfvén wave in an inhomogeneous plasma. *Physics of Plasmas*, *15*(6), 062901. https://doi.org/10.1063/1.2918742

Lysak, R. L., & Lotko, W. (1996). On the kinetic dispersion relation for shear Alfvén waves. *Journal of Geophysical Research*, *101*(A3), 5085–5094. https://doi.org/10.1029/95JA03712

Mauk, B. H., Haggerty, D. K., Jaskulek, S. E., Schlemm, C. E., Brown, L. E., Cooper, S. A., et al. (2017). The Jupiter Energetic Particle Detector Instrument (JEDI) investigation for the Juno Mission. *Space Science Reviews*, *213*(1–4), 289–346. https://doi.org/10.1007/s11214-013-0025-3

McComas, D. J., Alexander, N., Allegrini, F., Bagenal, F., Beebe, C., Clark, G., et al. (2017). The Jovian Auroral Distributions Experiment (JADE) on the Juno Mission to Jupiter. *Space Science Reviews*, *213*(1–4), 547–643. https://doi.org/10.1007/s11214-013-9990-9

Mura, A., Adriani, A., Connerney, J. E. P., Bolton, S., Altieri, F., Bagenal, F., et al. (2018). Juno observations of spot structures and a split tail in Io-induced aurorae on Jupiter. *Science*, *361*(6404), 774–777. https://doi.org/10.1126/science.aat1450

Neubauer, F. M. (1980). Nonlinear standing Alfvén wave current system at Io: Theory. *Journal of Geophysical Research*, *85*(A3), 1171–1178. https://doi.org/10.1029/JA085iA03p01171

Neubauer, F. M. (1998). The sub-Alfvénic interaction of the Galilean satellites with the Jovian magnetosphere. *Journal of Geophysical Research*, *103*(E9), 19843–19866. https://doi.org/10.1029/97JE03370

Ng, C. S., & Bhattacharjee, A. (1997). Scaling of anisotropic spectra due to the weak interaction of shear-Alfvén wave packets. *Physics of Plasmas*, *4*(3), 605–610. https://doi.org/10.1063/1.872158

Oughton, S., & Matthaeus, W. H. (2020). Critical balance and the physics of magnetohydrodynamic turbulence. *The Astrophysical Journal*, *897*(1), 37. https://doi.org/10.3847/1538-4357/ab8f2a

Piddington, J. H., & Drake, J. F. (1968). Electrodynamic effects of Jupiter's satellite Io. *Nature*, *217*(5132), 935–937. https://doi.org/10.1038/217935a0

Prangé, R., Rego, D., Southwood, D., Zarka, P., Miller, S., & Ip, W. (1996). Rapid energy dissipation and variability of the Io-Jupiter electrodynamic circuit. *Nature*, *380*(6573), 460. https://doi.org/10.1038/380460a0

Saur, J. (2004). Turbulent heating of Jupiter's middle magnetosphere. *The Astrophysical Journal*, *602*(2), L137–L140. https://doi.org/10.1086/382588

Saur, J. (2021). Turbulence in the magnetospheres of the outer planets. *Frontiers in Astronomy and Space Sciences*, *8*, 56. https://doi.org/10.3389/fspas.2021.624602

Saur, J., Grambusch, T., Duling, S., Neubauer, F. M., & Simon, S. (2013). Magnetic energy fluxes in sub-Alfvénic planet star and moon planet interactions. *Astronomy & Astrophysics*, *552*, A119. https://doi.org/10.1051/0004-6361/201118179

Saur, J., Janser, S., Schreiner, A., Clark, G., Mauk, B. H., Kollmann, P., et al. (2018). Wave-particle interaction of Alfvén waves in Jupiter's magnetosphere: Auroral and magnetospheric particle acceleration. *Journal of Geophysical Research: Space Physics*, *123*(11), 9560–9573. https://doi.org/10.1029/2018JA025948

Saur, J., Politano, H., Pouquet, A., & Matthaeus, W. H. (2002). Evidence for weak MHD turbulence in the middle magnetosphere of Jupiter. *Astronomy & Astrophysics*, *386*(2), 699–708. https://doi.org/10.1051/0004-6361:20020305

Schekochihin, A. A., Cowley, S. C., Dorland, W., Hammett, G. W., Howes, G. G., Quataert, E., & Tatsuno, T. (2009). Astrophysical gyrokinetics: Kinetic and fluid turbulent cascades in magnetized weakly collisional plasmas. *The Astrophysical Journal Supplement Series*, *182*(1), 310–377. https://doi.org/10.1088/0067-0049/182/1/310

Schreiner, A., & Saur, J. (2017). A model for dissipation of solar wind magnetic turbulence by kinetic Alfvén waves at electron scales: Comparison with observations. *The Astrophysical Journal*, *835*(2), 133. https://doi.org/10.3847/1538-4357/835/2/133

Stix, T. H. (1992). *Waves in plasmas*. Springer-Verlag.

Su, Y.-J., Ergun, R. E., Bagenal, F., & Delamere, P. A. (2003). Io-related Jovian auroral arcs: Modeling parallel electric fields. *Journal of Geophysical Research: Space Physics*, *108*(A2), 1094. https://doi.org/10.1029/2002JA009247

Su, Y.-J., Jones, S. T., Ergun, R. E., Bagenal, F., Parker, S. E., Delamere, P. A., & Lysak, R. L. (2006). Io-Jupiter interaction: Alfvén wave propagation and ionospheric Alfvén resonator. *Journal of Geophysical Research: Space Physics*, *111*(A6), A06211. https://doi.org/10.1029/2005JA011252

Sulaiman, A. H., Hospodarsky, G. B., Elliott, S. S., Kurth, W. S., Gurnett, D. A., Imai, M., et al. (2020). Wave-particle interactions associated with Io's auroral footprint: Evidence of Alfvén, ion cyclotron, and whistler modes. *Geophysical Research Letters*, *47*(22), e88432. https://doi.org/10.1029/2020GL088432

Szalay, J. R., Allegrini, F., Bagenal, F., Bolton, S. J., Bonfond, B., Clark, G., et al. (2020). A new framework to explain changes in Io's footprint tail electron fluxes. *Geophysical Research Letters*, *47*(18), e89267. https://doi.org/10.1029/2020GL089267

Szalay, J. R., Bagenal, F., Allegrini, F., Bonfond, B., Clark, G., Connerney, J. E. P., et al. (2020). Proton acceleration by Io's Alfvénic interaction. *Journal of Geophysical Research: Space Physics*, *125*(1), e27314. https://doi.org/10.1029/2019JA027314

Szalay, J. R., Bonfond, B., Allegrini, F., Bagenal, F., Bolton, S., Clark, G., et al. (2018). In situ observations connected to the Io footprint tail aurora. *Journal of Geophysical Research Planets*, *123*(11), 3061–3077. https://doi.org/10.1029/2018JE005752

Tao, C., Sahraoui, F., Fontaine, D., Patoul, J., Chust, T., Kasahara, S., & Retinò, A. (2015). Properties of Jupiter's magnetospheric turbulence observed by the Galileo spacecraft. *Journal of Geophysical Research: Space Physics*, *120*(4), 2477–2493. https://doi.org/10.1002/2014JA020749

von Papen, M., & Saur, J. (2015). Forward modeling of reduced power spectra from three-dimensional *k*-space. *The Astrophysical Journal*, *806*(1), 116. https://doi.org/10.1088/0004-637X/806/1/116

von Papen, M., Saur, J., & Alexandrova, O. (2014). Turbulent magnetic field fluctuations in Saturn's magnetosphere. *Journal of Geophysical Research: Space Physics*, *119*(4), 2797–2818. https://doi.org/10.1002/2013JA019542